Unimodular Sequence Design Based on Alternating Direction Method of Multipliers

Junli Liang, *Senior Member, IEEE*, Hing Cheung So, *Fellow, IEEE*, Jian Li, *Fellow, IEEE*, and Alfonso Farina, *Life Fellow, IEEE*

***Abstract*—The topic of probing waveform design has received considerable attention due to its numerous applications in active sensing. Apart from having the desirable property of constant magnitude, it is also anticipated that the designed sequence possesses low sidelobe autocorrelation and/or specified spectral shape. In this paper, the alternating direction method of multipliers (ADMM), which is a powerful variant of the augmented Lagrangian scheme for dealing with separable objective functions, is applied for synthesizing the probing sequences. To achieve impulse-like autocorrelation, we formulate the design problem as minimizing a nonlinear least-squares cost function in the frequency domain subject to the constraint that all sequence elements are of unit modulus. Via introducing auxiliary variables, we are able to separate the objective into linear and quadratic functions where the unimodular constraint is only imposed on the former, which results in an ADMM-style iterative procedure. In particular, fast implementation for the most computationally demanding step is investigated and local convergence of the ADMM method is proved. To deal with the spectral shape requirement, we borrow the concept in frequency-selective filter design where passband and stopband magnitudes are bounded to formulate the corresponding optimization problem. In this ADMM algorithm development, unit-step functions are utilized to transform the multivariable optimization into a quadratic polynomial problem with a single variable. The effectiveness of the proposed approach is demonstrated via computer simulations.**

***Index Terms*—Waveform design, unimodular waveform, low autocorrelation sidelobe, spectrally constrained waveform, alternating direction method of multipliers (ADMM), nonconvex optimization, active sensing.**

I. Introduction

ACTIVE sensing refers to finding valuable information of targets of interest or propagation medium via transmission of probing waveforms toward an inspected region as well as reception and analysis of the resultant reflected signals. The traditional sonar and radar application is to estimate the range and speed of a target from the round-trip time delay and Doppler frequency shift of the reflected waveform [1], [2]. It is also useful in many other fields including wireless communications and medical engineering [3], [4]. The performance of active sensing usually depends on two important factors, namely, transmit waveforms and receiver filters [5], and we will address the former in this work.

To maximize the achievable sensitivity and to obtain the best power efficiency through operating the power amplifiers in saturation, unimodularity or constant envelope has been a standard requirement in transmit sequence design [6], [7]. It is also desirable that the waveforms possess impulse-like autocorrelation [4]. For example, low autocorrelation sidelobes improve the target detection performance in radar range compression and ultrasonic imaging as well as facilitate synchronization in code division multiple access communication systems. On the other hand, designing waveforms with specified spectral shapes is required which is mainly driven by the spectrum congestion and competition issues [7]–[9]. In fact, the electromagnetic spectrum is already overcrowded due to the ever-growing demand of both high-quality wireless services and accurate remote sensing capabilities in telecommunication and radar systems. As a result, multiple users are forced to coexist within a finite spectrum allocation and one typical solution is to constrain the radar waveforms to have spectral nulls in specific bands to prevent interference with systems already operating in the corresponding frequencies [5].

There are two types of transmit waveforms, namely, aperiodic and periodic, needed in different applications. As autocorrelation function and power spectral density (PSD) form a Fourier transform pair, zero sidelobes in the time domain means a flat spectrum in the frequency domain. Based on this relationship, the cyclic algorithm-new (CAN) [10] and periodic CAN (PeCAN) [11], which are iterative techniques, have been developed to generate unimodular aperiodic and periodic sequences with low autocorrelation sidelobes, respectively. To design waveforms with arbitrarily spectral shapes, PeCAN has been modified as the SHAPE algorithm [5], [12]. Similar to the former, the latter introduces auxiliary phase (AP) variables and then determines the sequences and AP variables alternately. In [13], a majorization-minimization method which minimizes the integrated sidelobe level (ISL) for designing low sidelobe autocorrelation sequences and its modification incorporating the stopband attenuation in the frequency domain are developed. This approach is referred to as monotonic minimizer for ISL (MISL). Through unimodularity and spectral shape constraints, where flat spectrum is a special case, a Lagrange programming neural network (LPNN) algorithm [14], [15], which is based on nonlinear constrained optimization framework, has been

Manuscript received January 28, 2016; revised May 27, 2016; accepted July 10, 2016. Date of publication August 2, 2016; date of current version August 19, 2016. The associate editor coordinating the review of this manuscript and approving it for publication was Dr. Fauzia Ahmad. This work was supported in part by the National Natural Science Foundation of China under Grants 61471295 and 61172123 and in part by the Henry Fok Foundation under Grant 141119.

J. Liang is with the School of Electronics and Information, Northwestern Polytechnical University, Xi'an, Shaanxi 710072, China (e-mail: heery_2004@hotmail.com).

H. C. So is with the Department of Electronic Engineering, City University of Hong Kong, Hong Kong (e-mail: hcso@ee.cityu.edu.hk).

J. Li is with the Department of Electrical and Computer Engineering, University of Florida, Gainesville, FL 32611 USA (e-mail: li@dsp.ufl.edu).

A. Farina is with the IEEE AESS, Roma 00144, Italy (e-mail: alfonso.farina@outlook.it).

Color versions of one or more of the figures in this paper are available online at http://ieeexplore.ieee.org.

Digital Object Identifier 10.1109/TSP.2016.2597123

devised. In [16] and [17], radar waveform design subject to both constant modulus and similarity constraints is formulated as sequential optimization problems which are approximately solved by convex programming. Furthermore, stochastic optimization techniques [18]–[20] including evolutionary and particle swarm algorithms have been suggested.

On the other hand, the alternating direction method of multipliers (ADMM) [21], [22], which belongs to constrained optimization approaches, has received much attention because of its wide applicability to image reconstruction [23], distributed learning [24], sensor network localization [25], dimensionality reduction [26], just to name a few. In fact, there are two important and desirable features in ADMM. First, it decomposes a constrained convex optimization problem into multiple smaller subproblems whose solutions are coordinated to find the global optimum. This form of decomposition-coordination procedure allows parallel and/or distributed processing, and thus is well suited to the big data era. Second, in spite of employing iterations in the parameter updating process, it provides superior convergence properties. ADMM has also been applied to solve nonconvex problems and progress is continually made for the corresponding convergence analysis [27]. Motivated by the decomposability and superior convergence properties of ADMM, we devise a unimodular sequence design approach such that spectral shape constraint can be incorporated. The contributions of this work are highlighted as follows:

1) In the design formulation for unimodular waveforms with low sidelobe autocorrelation, the key difficulty is that the nonconvex unimodular constraints [28], [29] appear in the quadratic terms of the corresponding objective function. To circumvent this issue, we rewrite the objective via introducing auxiliary variables such that unimodularity is only imposed on the variables of the resultant linear terms. The two kinds of variables in the linear and quadratic components are determined alternately and iteratively according to ADMM.
2) In the proposed ADMM solution, one matrix inverse is needed at every iteration. We apply the matrix inverse lemma to accelerate the computation with the use of fast Fourier transform (FFT).
3) Our problem formulation facilitates the local convergence proof of the ADMM method via employing the results in [21], [22], [24].
4) The spectrally constrained waveform design problem, which is more challenging, is also solved by ADMM. Analogous to frequency-selective filter design, we allow passband and stopband tolerances in the frequency domain. In the algorithm development, unit-step functions are exploited to transform the original multivariable optimization into a quadratic polynomial problem with a single variable. Unlike existing solutions [5], [12]–[14], our approach can precisely control the passband ripples and stopband levels.

The rest of the paper is organized as follows. The problem of designing unimodular waveforms with impulse-like autocorrelation is formulated in Section II. In Section III, the ADMM solution is developed. The ADMM approach is also exploited for generalized spectrally constrained waveform design in Section IV. Numerical examples for contrasting the proposed approach with state-of-the-art algorithms are presented in Section V. Finally, conclusion is drawn in Section VI.

Notation: Vectors and matrices are denoted by boldface lowercase and uppercase letters, respectively. The $\|\cdot\|$ denotes the Frobenius norm while $(\cdot)^*$ is complex conjugate, $(\cdot)^T$ is transpose and $(\cdot)^H$ is Hermitian transpose. The $\mathbf{0}_n$, $\mathbf{1}_n$, and $\mathbf{I}_n$ represent the $n \times 1$ zero vector, $n \times 1$ vector of 1 and $n \times n$ identity matrix, respectively, while diag denotes diagonal matrix. The $\Re\{\}$ and $\Im\{\}$ mean the real and imaginary parts of a complex-valued scalar, vector or matrix.

II. Formulation of Low Sidelobe Autocorrelation Unimodular Sequence Design

In this section, we formulate the problem of designing unimodular sequences with low autocorrelation sidelobes. Let $\mathbf{x} = [x_0 \ \cdots \ x_{N-1}]^T \in \mathbb{C}^{N\times 1}$ be the uniformly-spaced sequence of length N to be designed. Without loss of generality, the unimodularity requirement here means that the sequence has a constant magnitude of one, that is:

$$|x_n| = 1, \quad n = 0, \ldots, N-1. \tag{1}$$

When $\mathbf{x}$ is periodic, its autocorrelation function, denoted by $\tilde{r}_k$, is defined as [4]:

$$\tilde{r}_k = \sum_{n=0}^{N-1} x_n x^*_{(n-k) \bmod N} = \tilde{r}^*_{-k}, \quad k = 0, \ldots, N-1, \tag{2}$$

where mod is the modulo operator. In a similar manner, the aperiodic autocorrelation function, denoted by r_k, is:

$$r_k = \sum_{n=k+1}^{N} x_n x^*_{n-k} = r^*_{-k}, \quad k = 0, \ldots, N-1. \tag{3}$$

We focus herein on the periodic waveform design and the development is readily applicable to aperiodic sequences. The standard approach to achieve impulse-like autocorrelation is to minimize the ISL, which is the sum of the squared magnitudes of all autocorrelation sidelobes. The design problem is then:

$$\begin{aligned} \min_{\mathbf{x}} \quad & \sum_{n=1}^{N-1} |\tilde{r}_k|^2 \\ \text{s.t.} \quad & |x_n| = 1, \quad n = 0, \ldots, N-1. \end{aligned} \tag{4}$$

Note that the MISL algorithm [13] has been developed for determining $\mathbf{x}$ according to (4). Making use of the Parseval's theorem, the ISL can be expressed in frequency domain [10], which results in the following equivalent problem:

$$\begin{aligned} \min_{\mathbf{x}} \quad & \sum_{n=0}^{N-1} \left(|X_n|^2 - N\right)^2 \\ \text{s.t.} \quad & |x_n| = 1, \quad n = 0, \ldots, N-1, \end{aligned} \tag{5}$$

where X_n represents the discrete Fourier transform (DFT) of $\mathbf{x}$ and has the form of:

$$X_n = \sum_{q=0}^{N-1} x_q e^{-j\frac{2\pi}{N}qn}, \quad n = 0, \ldots, N-1. \tag{6}$$

The two objective functions in (4)–(5) also align with the fundamental concept that zero autocorrelation sidelobes correspond to a flat PSD. From (5), it is seen that we basically need to make each $|X_n|^2$ close to the constant N. Based on this observation and in order to avoid minimizing the quartic function, the conventional variant of (5) is [10]:

$$\begin{aligned} \min_{\mathbf{x}} \quad & \sum_{n=0}^{N-1} \left(|X_n| - \sqrt{N}\right)^2 \\ \text{s.t.} \quad & |x_n| = 1, \quad n = 0, \ldots, N-1. \end{aligned} \tag{7}$$

In this work, we apply ADMM to find $\mathbf{x}$ from solving (7). Define the DFT vector $\mathbf{f}_n \in \mathbb{C}^{1\times N}$ whose kth element is:

$$\mathbf{f}_n(k) = e^{-j\frac{2\pi}{N}kn}, \quad n = 0, \ldots, N-1, \quad k = 0, \ldots, N-1. \tag{8}$$

With the use of (8), (6) can be written as

$$X_n = \mathbf{f}_n \mathbf{x}. \tag{9}$$

By introducing an auxiliary unimodular variable vector $\breve{\mathbf{x}} = [\breve{x}_0 \ \cdots \ \breve{x}_{N-1}]^T \in \mathbb{C}^{N\times 1}$, (7) can be rewritten as [4], [11]:

$$\begin{aligned} \min_{\mathbf{x},\breve{\mathbf{x}}} \quad & \|\mathbf{F}\mathbf{x} - \sqrt{N}\breve{\mathbf{x}}\|^2 \\ \text{s.t.} \quad & |x_n| = 1, \quad |\breve{x}_n| = 1, \quad n = 0, \ldots, N-1, \end{aligned} \tag{10}$$

where $\mathbf{F} = \left[\mathbf{f}_0^T \ \cdots \ \mathbf{f}_{N-1}^T\right]^T$. We further express (10) in a more compact form as

$$\begin{aligned} \min_{\mathbf{z}} \quad & \|\mathbf{A}\mathbf{z}\|^2 \\ \text{s.t.} \quad & |z_n| = 1, \quad n = 0, \ldots, 2N-1, \end{aligned} \tag{11}$$

where $\mathbf{z} = [\mathbf{x}^T \ \breve{\mathbf{x}}^T]^T$ and $\mathbf{A} = [\mathbf{F} \ -\sqrt{N}\mathbf{I}_N]$.

Analogous to (7), the corresponding aperiodic waveform design formulation is [4], [10]:

$$\begin{aligned} \min_{\mathbf{x}} \quad & \sum_{n=0}^{2N-1} \left(|\tilde{X}_n| - \sqrt{N}\right)^2 \\ \text{s.t.} \quad & |x_n| = 1, \quad n = 0, \ldots, N-1. \end{aligned} \tag{12}$$

where $\tilde{X}_n$ is the DFT of $[\mathbf{x}^T \ \ \mathbf{0}_N^T]^T$, and we can follow the same procedure to convert (12) to a compact form similar to (11) [4], [10], [11].

III. Algorithm Development

It is apparent that if $\mathbf{z}$ is a solution to (11), then $e^{j\theta}\mathbf{z}$, where $\theta \in [0, 2\pi]$ is an arbitrary phase angle, is also a solution, which indicates the phase ambiguity problem. More important, (11) is a nonconvex problem because the constraints are not convex due to the fact that the feasible region is the union of $2N$ circles. To address these issues, we start assigning the first element of $\mathbf{z}$ to be one, namely, $z_0 = 1$. We further define $\breve{\mathbf{z}} = [z_1 \ \cdots \ z_{2N-1}]^T \in \mathbb{C}^{(2N-1)\times 1}$ with $\mathbf{z} = [1 \ \breve{\mathbf{z}}^T]^T$, and decompose $\mathbf{A}$ as $\mathbf{A} = [\mathbf{a}_1 \ \mathbf{A}_2]$ where $\mathbf{a}_1 \in \mathbb{C}^{N\times 1}$ is its first column and $\mathbf{A}_2 \in \mathbb{C}^{N\times(2N-1)}$ is the remaining component. Then, (11) can be rewritten in an equivalent form as:

$$\begin{aligned} \min_{\breve{\mathbf{z}}} \quad & \breve{\mathbf{z}}^H \mathbf{A}_2^H \mathbf{A}_2 \breve{\mathbf{z}} + \breve{\mathbf{z}}^H \mathbf{A}_2^H \mathbf{a}_1 + \mathbf{a}_1^H \mathbf{A}_2 \breve{\mathbf{z}} + \mathbf{a}_1^H \mathbf{a}_1 \\ \text{s.t.} \quad & |z_n| = 1, \quad n = 1, \ldots, 2N-1. \end{aligned} \tag{13}$$

By comparing (11) with (13), it is seen that unlike the former objective function where there is only one quadratic function $\mathbf{z}^H\mathbf{A}^H\mathbf{A}\mathbf{z}$ such that $2N$ unimodulus constraints are imposed on $\mathbf{z}$, the latter contains the linear term $\breve{\mathbf{z}}^H\mathbf{A}_2^H\mathbf{a}_1 + \mathbf{a}_1^H\mathbf{A}_2\breve{\mathbf{z}}$ and the quadratic component $\breve{\mathbf{z}}^H\mathbf{A}_2^H\mathbf{A}_2\breve{\mathbf{z}}$. It can be seen that if the unimodular constraints only appear in the linear term of (13), then the resultant problem will be easily handled. Therefore, we apply the variable splitting trick and introduce the auxiliary variable vector $\breve{\mathbf{y}} = [y_1 \ \cdots \ y_{2N-1}]^T \in \mathbb{C}^{(2N-1)\times 1}$ with the constraint $\breve{\mathbf{y}} = \breve{\mathbf{z}}$ to convert (13) as:

$$\begin{aligned} \min_{\breve{\mathbf{y}},\breve{\mathbf{z}}} \quad & \breve{\mathbf{y}}^H \mathbf{A}_2^H \mathbf{A}_2 \breve{\mathbf{y}} + \breve{\mathbf{z}}^H \mathbf{A}_2^H \mathbf{a}_1 + \mathbf{a}_1^H \mathbf{A}_2 \breve{\mathbf{z}} \\ \text{s.t.} \quad & \breve{\mathbf{y}} = \breve{\mathbf{z}}, \\ & |z_n| = 1, \quad n = 1, \ldots, 2N-1, \end{aligned} \tag{14}$$

where the irrelevant constant term $\mathbf{a}_1^H\mathbf{a}_1$ is removed. Contrasting (13) and (14), we note that the introduction of $\breve{\mathbf{y}}$ enables the nonconvex constraints to appear only on the linear term in the objective function of (14), and also there is no constraint on the quadratic term, simplifying the problem to solve.

ADMM blends the decomposability of dual ascent with the superior convergence property of the multiplier method. We exploit this property to solve (14). Since ADMM is a real-valued implementation method [21], [22], [24], we transform (14) using the real-valued expressions as follows.

Let $\mathbf{A}_{2,r} = \Re\{\mathbf{A}_2\}, \mathbf{A}_{2,i} = \Im\{\mathbf{A}_2\}, \bar{\mathbf{z}} = [(\Re\{\breve{\mathbf{z}}\})^T \ (\Im\{\breve{\mathbf{z}}\})^T]^T$ and $\bar{\mathbf{y}} = [(\Re\{\breve{\mathbf{y}}\})^T \ (\Im\{\breve{\mathbf{y}}\})^T]^T$. Then (14) can be expressed as:

$$\begin{aligned} \min_{\bar{\mathbf{z}},\bar{\mathbf{y}}} \quad & \bar{\mathbf{y}}^T \mathbf{H} \bar{\mathbf{y}} + 2\mathbf{c}^T \bar{\mathbf{z}} \\ \text{s.t.} \quad & \bar{\mathbf{y}} = \bar{\mathbf{z}}, \\ & z_{n,r}^2 + z_{n,i}^2 = 1, \quad n = 1, \ldots, 2N-1, \end{aligned} \tag{15}$$

where $z_{n,r} = \Re\{z_n\}$ and $z_{n,i} = \Im\{z_n\}$ are the nth and $(n + 2N - 1)$th elements of $\bar{\mathbf{z}}$, respectively. Moreover, $\mathbf{H}$ and $\mathbf{c}$ have the forms:

$$\begin{aligned} \mathbf{H} = & [\mathbf{A}_{2,r} \quad -\mathbf{A}_{2,i}]^T [\mathbf{A}_{2,r} \quad -\mathbf{A}_{2,i}] \\ & + [\mathbf{A}_{2,i} \quad \mathbf{A}_{2,r}]^T [\mathbf{A}_{2,i} \quad \mathbf{A}_{2,r}], \end{aligned} \tag{16}$$

and

$$\mathbf{c} = \left[\Re\{\mathbf{a}_1^H\mathbf{A}_2\} \quad -\Im\{\mathbf{a}_1^H\mathbf{A}_2\}\right]^T. \tag{17}$$

Note that the constraints $z_{n,r}^2 + z_{n,i}^2 = 1$, $n = 1, \ldots, 2N - 1$, are imposed on $\bar{\mathbf{z}}$ and are not related to $\bar{\mathbf{y}}$. Hence they play their roles only in the step of finding $\bar{\mathbf{z}}$. For this reason, we devise the augmented Lagrangian:

$$\mathcal{L}_\rho(\bar{\mathbf{y}}, \bar{\mathbf{z}}, \boldsymbol{\lambda}) = \bar{\mathbf{y}}^T \mathbf{H} \bar{\mathbf{y}} + 2\mathbf{c}^T \bar{\mathbf{z}} + \boldsymbol{\lambda}^T (\bar{\mathbf{y}} - \bar{\mathbf{z}}) + \frac{\rho}{2}\|\bar{\mathbf{y}} - \bar{\mathbf{z}}\|^2, \tag{18}$$

where $\rho > 0$ and $\boldsymbol{\lambda} \in \mathbb{R}^{(4N-2)\times 1}$ are the step size and Lagrange multiplier vector [21], [22], [24], respectively.

Based on the decomposition-coordination procedure of the ADMM, we then determine $\{\bar{\mathbf{y}}, \bar{\mathbf{z}}, \boldsymbol{\lambda}\}$ from (18) via the following steps:

1) With the obtained $\{\bar{\mathbf{y}}(t), \boldsymbol{\lambda}(t)\}$ at the tth iteration, compute $\bar{\mathbf{z}}(t+1)$ using:

$$\begin{aligned}\bar{\mathbf{z}}(t+1) &= \arg\min_{\bar{\mathbf{z}}} \quad \mathcal{L}_\rho(\bar{\mathbf{y}}(t), \bar{\mathbf{z}}, \boldsymbol{\lambda}(t)),\\ &= \arg\min_{\bar{\mathbf{z}}} \quad \mathbf{q}^T(t+1)\bar{\mathbf{z}} + \frac{\rho}{2}\bar{\mathbf{z}}^T\bar{\mathbf{z}},\\ \text{s.t.} \quad & z_{n,r}^2 + z_{n,i}^2 = 1, \quad n = 1, \ldots, 2N-1, \end{aligned} \tag{19}$$

where

$$\mathbf{q}(t+1) = 2\mathbf{c} - \boldsymbol{\lambda}(t) - \rho\bar{\mathbf{y}}(t). \tag{20}$$

Lemma 1: (19) is equivalent to the following optimization problem with a linear objective function:

$$\begin{aligned}\min_{\bar{\mathbf{z}}} \quad & \mathbf{q}^T(t+1)\bar{\mathbf{z}},\\ \text{s.t.} \quad & z_{n,r}^2 + z_{n,i}^2 = 1, \quad n = 1, \ldots, 2N-1. \end{aligned} \tag{21}$$

Proof: The constraints $z_{n,r}^2 + z_{n,i}^2 = 1,\ n = 1, \ldots, 2N-1$ give $\bar{\mathbf{z}}^T\bar{\mathbf{z}} = 2N-1$. When the constraints are satisfied, (19) is equivalent to (21). The proof is complete. ■

As shown in (21), the nonconvex constraints $z_{n,r}^2 + z_{n,i}^2 = 1,\ n = 1, \ldots, 2N-1$, are enforced on the linear function $\mathbf{q}^T(t+1)\bar{\mathbf{z}}$ only, which simplifies the computations. Furthermore, (21) can be decomposed into $2N-1$ subproblems for the variable pair $\{z_{n,r}, z_{n,i}\},\ n = 1, \ldots, 2N-1$:

$$\begin{aligned}\min_{z_{n,r}, z_{n,i}} \quad & \xi_n z_{n,r} + \beta_n z_{n,i}\\ \text{s.t.} \quad & z_{n,r}^2 + z_{n,i}^2 = 1, \quad n = 1, \ldots, 2N-1, \end{aligned} \tag{22}$$

where ξ_n and β_n are the nth and $(2N-1+n)$th elements of $\mathbf{q}(t+1)$, respectively. Applying the method of Langrange multiplers, we convert (22) to

$$\begin{aligned}\min_{z_{n,r}, z_{n,i}, \kappa_n} \mathcal{L}_n(z_{n,r}, z_{n,i}, \kappa_n) &= \xi_n z_{n,r} + \beta_n z_{n,i}\\ + \kappa_n\left(z_{n,r}^2 + z_{n,i}^2 - 1\right), &\quad n = 1, \ldots, 2N-1, \end{aligned} \tag{23}$$

where κ_n denotes the multiplier corresponding to the constraint $z_{n,r}^2 + z_{n,i}^2 = 1$.

Taking the partial derivatives of $\mathcal{L}_n(z_{n,r}, z_{n,i}, \kappa_n)$ with respect to $z_{n,r}$ and $z_{n,i}$ and then setting the resultant expressions to zero yield

$$\xi_n + 2\kappa_n z_{n,r} = 0, \tag{24}$$

and

$$\beta_n + 2\kappa_n z_{n,i} = 0. \tag{25}$$

Then, we substitute

$$z_{n,r}(t+1) = -\frac{\xi_n}{2\kappa_n}, \quad z_{n,i}(t+1) = -\frac{\beta_n}{2\kappa_n}, \tag{26}$$

into the constraint $z_{n,r}^2 + z_{n,i}^2 = 1$ to obtain

$$\xi_n^2 + \beta_n^2 = 4\kappa_n^2. \tag{27}$$

Apparently, there are two possible values of κ_n:

$$\kappa_n = \pm\sqrt{\xi_n^2 + \beta_n^2}/2. \tag{28}$$

Inserting $\kappa_n = \frac{\sqrt{\xi_n^2+\beta_n^2}}{2}$ and $\kappa_n = -\frac{\sqrt{\xi_n^2+\beta_n^2}}{2}$ into the objective function $\xi_n z_{n,r} + \beta_n z_{n,i}$ in (22), we have $-\sqrt{\xi_n^2+\beta_n^2}$ and $\sqrt{\xi_n^2+\beta_n^2}$, respectively. It is easy to deduce that the correct Lagrange multiplier should be the former. Thus, the solution to (22) is obtained by substituting $\kappa_n = \frac{\sqrt{\xi_n^2+\beta_n^2}}{2}$ into (26).

2) Compute $\bar{\mathbf{y}}(t+1)$ by solving the following optimization problem with $\{\bar{\mathbf{z}}(t+1), \boldsymbol{\lambda}(t)\}$:

$$\begin{aligned}\bar{\mathbf{y}}(t+1) &= \arg\min_{\bar{\mathbf{y}}} \mathcal{L}_\rho(\bar{\mathbf{y}}, \bar{\mathbf{z}}(t+1), \boldsymbol{\lambda}(t))\\ &= \arg\min_{\bar{\mathbf{y}}} \bar{\mathbf{y}}^T\bar{\mathbf{H}}\bar{\mathbf{y}} + 2\mathbf{d}^T(t+1)\bar{\mathbf{y}}, \end{aligned} \tag{29}$$

where

$$\bar{\mathbf{H}} = \mathbf{H} + \frac{\rho}{2}\mathbf{I}_{4N-2}, \tag{30}$$

and

$$\mathbf{d}(t+1) = \frac{1}{2}(\boldsymbol{\lambda}(t) - \rho\bar{\mathbf{z}}(t+1)). \tag{31}$$

The solution to (29) is then:

$$\bar{\mathbf{y}}(t+1) = -\bar{\mathbf{H}}^{-1}\mathbf{d}(t+1), \tag{32}$$

which requires $(4N-2)^2$ multiplications. Nevertheless, we have provided a fast algorithm for computing (32) via FFT in Appendix A.

3) Compute $\boldsymbol{\lambda}(t+1)$ using:

$$\boldsymbol{\lambda}(t+1) = \boldsymbol{\lambda}(t) + \rho\left(\bar{\mathbf{y}}(t+1) - \bar{\mathbf{z}}(t+1)\right). \tag{33}$$

Steps 1) to 3) are repeated until a stopping criterion is reached, e.g., a maximum iteration number T is attained and/or $\max|\bar{\mathbf{y}}(t+1) - \bar{\mathbf{z}}(t+1)| < \delta$ where $\delta > 0$ is a small tolerance parameter [21], [22], [24]. The local convergence proof of the proposed ADMM algorithm is provided in Appendix B. Since (7) and (12) are similar, we can modify Steps 1) to 3) accordingly for the synthesis of aperiodic unimodular waveforms with low autocorrelation sidelobes.

IV. Generalized Spectrally Constrained Waveform Design

In addition to the low sidelobe autocorrelation requirement, there is need for the magnitude spectrum of $\mathbf{x}$ to satisfy a specified shape other than a rectangular pulse. For ease of description, in terms of the filter design notion, we call the available and avoided spectrum regions as the passband and stopband, respectively. Divide the entire frequency region into N uniformly-spaced frequency grid points and among them there are P and S points in the passband and stopband, respectively, such that $P + S = N$. For all the P frequency grids within the passband, let $\tilde{\mathbf{f}}_p$ be the corresponding DFT vector. The power spectrum in this range should satisfy $(1-r)\alpha \le \mathbf{x}^H\tilde{\mathbf{f}}_p^H\tilde{\mathbf{f}}_p\mathbf{x} \le (1+r)\alpha$ for $p = 1, \ldots, P$, where $\alpha > 0$ is a scalar and $1 > r > 0$ is the ripple term. Moreover, for all the S frequency grids within the stopband, the power spectrum should satisfy $\mathbf{x}^H\hat{\mathbf{f}}_s^H\hat{\mathbf{f}}_s\mathbf{x} \le \eta\alpha$

for $s = 1, \ldots, S$, where η is the sidelobe level and $\hat{\mathbf{f}}_s$ is the corresponding DFT vector. For this generalized spectrally constrained unimodular waveform design problem, there are many solutions due to different choices of α. Yet, the excessively large power spectrum is not expected. Therefore, we select the solution with the smallest α in the region $[\alpha_L, \alpha_U]$ for the spectral constraints, which may be pre-determined according to the Parseval's theorem and the two-sided bounds or region of interest. As a result, the generalized spectrally constrained waveform design problem is formulated as follows:

$$\begin{aligned} \min_{\mathbf{x},\alpha} \quad & \alpha \\ \text{s.t.} \quad & |x_n| = 1, \quad n = 0, \ldots, N-1, \\ & (1-r)\alpha \le \mathbf{x}^H \tilde{\mathbf{f}}_p^H \tilde{\mathbf{f}}_p \mathbf{x} \le (1+r)\alpha, \quad p = 1, \ldots, P, \\ & \mathbf{x}^H \hat{\mathbf{f}}_s^H \hat{\mathbf{f}}_s \mathbf{x} \le \eta\alpha, \quad s = 1, \ldots, S, \\ & \alpha \in [\alpha_L, \alpha_U]. \end{aligned} \tag{34}$$

Again, (34) is a nonconvex optimization problem due to the unimodular constraint and $(1-r)\alpha \le \mathbf{x}^H \tilde{\mathbf{f}}_p^H \tilde{\mathbf{f}}_p \mathbf{x}$. To apply the ADMM method, we first transform (34) into the following real-valued optimization problem:

$$\begin{aligned} \min_{\bar{\mathbf{x}},\alpha} \quad & \alpha \\ \text{s.t.} \quad & \bar{x}_n^2 + \bar{x}_{n+N}^2 = 1, \quad n = 0, \ldots, N-1, \\ & (1-r)\alpha \le \bar{\mathbf{x}}^T \tilde{\mathbf{F}}_p^T \tilde{\mathbf{F}}_p \bar{\mathbf{x}} \le (1+r)\alpha, \quad p = 1, \ldots, P, \\ & \bar{\mathbf{x}}^T \hat{\mathbf{F}}_s^T \hat{\mathbf{F}}_s \bar{\mathbf{x}} \le \eta\alpha, \quad s = 1, \ldots, S, \\ & \alpha \in [\alpha_L, \alpha_U], \end{aligned} \tag{35}$$

where

$$\tilde{\mathbf{F}}_p = \begin{bmatrix} \Re\{\tilde{\mathbf{f}}_p\} & -\Im\{\tilde{\mathbf{f}}_p\} \\ \Im\{\tilde{\mathbf{f}}_p\} & \Re\{\tilde{\mathbf{f}}_p\} \end{bmatrix}, \quad p = 1, \ldots, P, \tag{36}$$

$$\hat{\mathbf{F}}_s = \begin{bmatrix} \Re\{\hat{\mathbf{f}}_s\} & -\Im\{\hat{\mathbf{f}}_s\} \\ \Im\{\hat{\mathbf{f}}_s\} & \Re\{\hat{\mathbf{f}}_s\} \end{bmatrix}, \quad s = 1, \ldots, S, \tag{37}$$

$$\bar{\mathbf{x}} = \left[(\Re\{\mathbf{x}\})^T \quad (\Im\{\mathbf{x}\})^T \right]^T, \tag{38}$$

and $\bar{x}_n$ is the nth element of $\bar{\mathbf{x}}$ for $n = 0, \ldots, 2N-1$. Similarly, with the use of variable splitting, we define

$$\mathbf{v}_p = \tilde{\mathbf{F}}_p \bar{\mathbf{x}},\ \mathbf{w}_s = \hat{\mathbf{F}}_s \bar{\mathbf{x}},\ p = 1, \ldots, P,\ s = 1, \ldots, S. \tag{39}$$

Then (35) can be rewritten as:

$$\begin{aligned} \min_{\bar{\mathbf{x}},\alpha,\mathbf{v}_p,\mathbf{w}_s} \quad & \alpha \\ \text{s.t.} \quad & \bar{x}_n^2 + \bar{x}_{n+N}^2 = 1, \quad n = 0, \ldots, N-1, \\ & \mathbf{v}_p = \tilde{\mathbf{F}}_p \bar{\mathbf{x}}, \quad p = 1, \ldots, P, \\ & \mathbf{w}_s = \hat{\mathbf{F}}_s \bar{\mathbf{x}}, \quad s = 1, \ldots, S, \\ & (1-r)\alpha \le \|\mathbf{v}_p\|^2 \le (1+r)\alpha, \quad p = 1, \ldots, P, \\ & \|\mathbf{w}_s\|^2 \le \eta\alpha, \quad s = 1, \ldots, S, \\ & \alpha \in [\alpha_L, \alpha_U]. \end{aligned} \tag{40}$$

Similar to (18), the constraints $\bar{x}_n^2 + \bar{x}_{n+N}^2 = 1$, $(1-r)\alpha \le \|\mathbf{v}_p\|^2 \le (1+r)\alpha$, $\|\mathbf{w}_s\|^2 \le \eta\alpha$, and $\alpha \in [\alpha_L, \alpha_U]$ on $\bar{\mathbf{x}}$, $\mathbf{v}_p$, $\mathbf{w}_s$, and α will play their roles in the corresponding variable determination steps. Thus, the augmented Lagrangian from (40) is devised as follows:

$$\begin{aligned} \mathcal{L}_\rho(\bar{\mathbf{x}}, \alpha, \mathbf{v}_p, \mathbf{w}_s, \boldsymbol{\lambda}_{1,p}, \boldsymbol{\lambda}_{2,s}) &= \alpha \\ &+ \sum_{p=1}^{P} \boldsymbol{\lambda}_{1,p}^T \left(\mathbf{v}_p - \tilde{\mathbf{F}}_p \bar{\mathbf{x}}\right) + \sum_{p=1}^{P} \frac{\rho}{2} \|\mathbf{v}_p - \tilde{\mathbf{F}}_p \bar{\mathbf{x}}\|^2 \\ &+ \sum_{s=1}^{S} \boldsymbol{\lambda}_{2,s}^T \left(\mathbf{w}_s - \hat{\mathbf{F}}_s \bar{\mathbf{x}}\right) + \sum_{s=1}^{S} \frac{\rho}{2} \|\mathbf{w}_s - \hat{\mathbf{F}}_s \bar{\mathbf{x}}\|^2. \end{aligned} \tag{41}$$

Employing ADMM, we determine $\{\bar{\mathbf{x}}, \alpha, \mathbf{v}_p, \mathbf{w}_s, \boldsymbol{\lambda}_{1,p}, \boldsymbol{\lambda}_{2,s}\}$ via the following alternating iterative steps:

1) Determine $\bar{\mathbf{x}}(t+1)$ with the obtained $\{\alpha(t), \mathbf{v}_p(t), \mathbf{w}_s(t), \boldsymbol{\lambda}_{1,p}(t), \boldsymbol{\lambda}_{2,s}(t)\}$ using:

$$\begin{aligned} &\min_{\bar{\mathbf{x}}} \ \mathcal{L}_\rho(\bar{\mathbf{x}}, \alpha(t), \mathbf{v}_p(t), \mathbf{w}_s(t), \boldsymbol{\lambda}_{1,p}(t), \boldsymbol{\lambda}_{2,s}(t)) \\ &= \min_{\bar{\mathbf{x}}} \ \alpha(t) \\ &\quad + \sum_{p=1}^{P} \boldsymbol{\lambda}_{1,p}^T(t) \left(\mathbf{v}_p(t) - \tilde{\mathbf{F}}_p \bar{\mathbf{x}}\right) + \sum_{p=1}^{P} \frac{\rho}{2} \|\mathbf{v}_p(t) - \tilde{\mathbf{F}}_p \bar{\mathbf{x}}\|^2 \\ &\quad + \sum_{s=1}^{S} \boldsymbol{\lambda}_{2,s}^T(t) \left(\mathbf{w}_s(t) - \hat{\mathbf{F}}_s \bar{\mathbf{x}}\right) + \sum_{s=1}^{S} \frac{\rho}{2} \|\mathbf{w}_s(t) - \hat{\mathbf{F}}_s \bar{\mathbf{x}}\|^2 \\ &\text{s.t.} \quad \bar{x}_n^2 + \bar{x}_{n+N}^2 = 1, \quad n = 0, \ldots, N-1. \end{aligned} \tag{42}$$

Ignoring the constant term, (42) is simplified as:

$$\begin{aligned} \min_{\bar{\mathbf{x}}} \quad & \bar{\mathbf{x}}^T \mathbf{R} \bar{\mathbf{x}} + \bar{\mathbf{d}}^T(t+1) \bar{\mathbf{x}} \\ \text{s.t.} \quad & \bar{x}_n^2 + \bar{x}_{n+N}^2 = 1, \quad n = 0, \ldots, N-1, \end{aligned} \tag{43}$$

where

$$\begin{aligned} \bar{\mathbf{d}}(t+1) = &\sum_{p=1}^{P} \left(-\tilde{\mathbf{F}}_p^T \boldsymbol{\lambda}_{1,p}(t) - \rho \tilde{\mathbf{F}}_p^T \mathbf{v}_p(t)\right) \\ &+ \sum_{s=1}^{S} \left(-\hat{\mathbf{F}}_s^T \boldsymbol{\lambda}_{2,s}(t) - \rho \hat{\mathbf{F}}_s^T \mathbf{w}_s(t)\right). \end{aligned} \tag{44}$$

Since $\mathbf{R} = \sum_{p=1}^{P} \tilde{\mathbf{F}}_p^T \tilde{\mathbf{F}}_p + \sum_{s=1}^{S} \hat{\mathbf{F}}_s^T \hat{\mathbf{F}}_s = N\mathbf{I}_{2N}$ and $\bar{\mathbf{x}}^T \mathbf{R} \bar{\mathbf{x}} = N^2$, (43) is equivalent to

$$\begin{aligned} \min_{\bar{\mathbf{x}}} \quad & \bar{\mathbf{d}}^T(t+1) \bar{\mathbf{x}} \\ \text{s.t.} \quad & \bar{x}_n^2 + \bar{x}_{n+N}^2 = 1, \quad n = 0, \ldots, N-1, \end{aligned} \tag{45}$$

which can be solved by the similar steps in (22)–(28).

2) Determine $\{\alpha(t+1), \mathbf{v}_p(t+1), \mathbf{w}_s(t+1)\}$ with the obtained $\{\bar{\mathbf{x}}(t+1), \boldsymbol{\lambda}_{1,p}(t), \boldsymbol{\lambda}_{2,s}(t)\}$ from:

$$\begin{aligned}
&\min_{\alpha,\mathbf{v}_p,\mathbf{w}_s} \mathcal{L}_\rho\left(\bar{\mathbf{x}}(t+1), \alpha, \mathbf{v}_p, \mathbf{w}_s, \boldsymbol{\lambda}_{1,p}(t), \boldsymbol{\lambda}_{2,s}(t)\right)\\
&= \min_{\alpha,\mathbf{v}_p,\mathbf{w}_s} \alpha + \sum_{p=1}^{P} \boldsymbol{\lambda}_{1,p}^T(t)\big(\mathbf{v}_p - \tilde{\mathbf{F}}_p\bar{\mathbf{x}}(t+1)\big)\\
&\quad + \sum_{p=1}^{P} \frac{\rho}{2}\|\mathbf{v}_p - \tilde{\mathbf{F}}_p\bar{\mathbf{x}}(t+1)\|^2\\
&\quad + \sum_{s=1}^{S} \boldsymbol{\lambda}_{2,s}^T(t)\big(\mathbf{w}_s - \hat{\mathbf{F}}_s\bar{\mathbf{x}}(t+1)\big)\\
&\quad + \sum_{s=1}^{S} \frac{\rho}{2}\|\mathbf{w}_s - \hat{\mathbf{F}}_s\bar{\mathbf{x}}(t+1)\|^2,\\
&\text{s.t.} \quad (1-r)\alpha \le \|\mathbf{v}_p\|^2 \le (1+r)\alpha, \quad p = 1,\ldots,P,\\
&\qquad \|\mathbf{w}_s\|^2 \le \eta\alpha, \quad s = 1,\ldots,S,\\
&\qquad \alpha \in [\alpha_L, \alpha_U]. \qquad (46)
\end{aligned}$$

Define

$$\tilde{\mathbf{v}}_p(t+1) = \tilde{\mathbf{F}}_p\bar{\mathbf{x}}(t+1) - \frac{1}{\rho}\boldsymbol{\lambda}_{1,p}(t), \quad p = 1,\ldots,P, \qquad (47)$$

$$\tilde{\mathbf{w}}_s(t+1) = \hat{\mathbf{F}}_s\bar{\mathbf{x}}(t+1) - \frac{1}{\rho}\boldsymbol{\lambda}_{2,s}(t), \quad s = 1,\ldots,S. \qquad (48)$$

Then (46) can be simplified as:

$$\begin{aligned}
&\min_{\alpha,\mathbf{v}_p,\mathbf{w}_s} \quad \alpha + \sum_{p=1}^{P} \frac{\rho}{2}\|\mathbf{v}_p - \tilde{\mathbf{v}}_p(t+1)\|^2\\
&\qquad\qquad + \sum_{s=1}^{S} \frac{\rho}{2}\|\mathbf{w}_s - \tilde{\mathbf{w}}_s(t+1)\|^2,\\
&\text{s.t.} \quad (1-r)\alpha \le \|\mathbf{v}_p\|^2 \le (1+r)\alpha, \quad p = 1,\ldots,P,\\
&\qquad \|\mathbf{w}_s\|^2 \le \eta\alpha, \quad s = 1,\ldots,S,\\
&\qquad \alpha \in [\alpha_L, \alpha_U]. \qquad (49)
\end{aligned}$$

Obviously, α is coupled with $\mathbf{v}_p$ and $\mathbf{w}_s$ due to the constraints $(1-r)\alpha \le \|\mathbf{v}_p\|^2 \le (1+r)\alpha$ and $\|\mathbf{w}_s\|^2 \le \eta\alpha$. However, once α is provided, the optimal $\mathbf{v}_p(t+1)$ and $\mathbf{w}_s(t+1)$ are given by:

$$\begin{aligned}
&\mathbf{v}_p(t+1)\\
&= \begin{cases} \frac{\sqrt{(1+r)\alpha}}{\|\tilde{\mathbf{v}}_p(t+1)\|}\tilde{\mathbf{v}}_p(t+1), & \|\tilde{\mathbf{v}}_p(t+1)\| \ge \sqrt{(1+r)\alpha}\\ \frac{\sqrt{(1-r)\alpha}}{\|\tilde{\mathbf{v}}_p(t+1)\|}\tilde{\mathbf{v}}_p(t+1), & \|\tilde{\mathbf{v}}_p(t+1)\| \le \sqrt{(1-r)\alpha},\\ \tilde{\mathbf{v}}_p(t+1), & \text{otherwise} \end{cases} \qquad (50)
\end{aligned}$$

and

$$\begin{aligned}
&\mathbf{w}_s(t+1)\\
&= \begin{cases} \frac{\sqrt{\eta\alpha}}{\|\tilde{\mathbf{w}}_s(t+1)\|}\tilde{\mathbf{w}}_s(t+1), & \|\tilde{\mathbf{w}}_s(t+1)\| \ge \sqrt{\eta\alpha}\\ \tilde{\mathbf{w}}_s(t+1), & \text{otherwise} \end{cases}. \qquad (51)
\end{aligned}$$

Additionally, the term $\|\mathbf{v}_p - \tilde{\mathbf{v}}_p(t+1)\|^2$ and $\|\mathbf{w}_s - \tilde{\mathbf{w}}_s(t+1)\|^2$ can be transformed into the functions of α as shown in (52) at the bottom of this page.

$$\begin{aligned}
&\|\mathbf{w}_s - \tilde{\mathbf{w}}_s(t+1)\|^2\\
&= \begin{cases} (\sqrt{\eta\alpha} - \|\tilde{\mathbf{w}}_s(t+1)\|)^2, & \|\tilde{\mathbf{w}}_s(t+1)\| \ge \sqrt{\eta\alpha}\\ 0 & \text{otherwise} \end{cases}. \qquad (53)
\end{aligned}$$

As a result, we convert (49) into an optimization problem with a single variable α. To proceed, we define three unit-step functions as follows:

$$\begin{aligned}
&S_1(\tilde{\mathbf{v}}_p(t+1), (1+r)\alpha)\\
&= \begin{cases} 1, & \|\tilde{\mathbf{v}}_p(t+1)\| \ge \sqrt{(1+r)\alpha}\\ 0, & \text{otherwise} \end{cases}, \qquad (54)\\
&S_2(\tilde{\mathbf{v}}_p(t+1), (1-r)\alpha)\\
&= \begin{cases} 1, & \|\tilde{\mathbf{v}}_p(t+1)\| \le \sqrt{(1-r)\alpha}\\ 0, & \text{otherwise} \end{cases}, \qquad (55)
\end{aligned}$$

and

$$\begin{aligned}
&S_3(\tilde{\mathbf{w}}_s(t+1), \eta\alpha)\\
&= \begin{cases} 1 & \|\tilde{\mathbf{w}}_s(t+1)\| \ge \sqrt{\eta\alpha}\\ 0 & \text{otherwise} \end{cases}. \qquad (56)
\end{aligned}$$

$$\|\mathbf{v}_p - \tilde{\mathbf{v}}_p(t+1)\|^2 = \begin{cases} (\sqrt{(1+r)\alpha} - \|\tilde{\mathbf{v}}_p(t+1)\|)^2, & \|\tilde{\mathbf{v}}_p(t+1)\| \ge \sqrt{(1+r)\alpha}\\ (\sqrt{(1-r)\alpha} - \|\tilde{\mathbf{v}}_p(t+1)\|)^2, & \|\tilde{\mathbf{v}}_p(t+1)\| \le \sqrt{(1-r)\alpha}\\ 0, & \text{otherwise} \end{cases}, \qquad (52)$$

Employing (54)–(56), (49) can be rewritten as:

$$\begin{aligned}\min_{\alpha}\quad & \alpha+\sum_{p=1}^{P}\frac{\rho}{2}S_1(\tilde{\mathbf{v}}_p(t+1),(1+r)\alpha)\\ &\times\left(\sqrt{(1+r)\alpha}-\|\tilde{\mathbf{v}}_p(t+1)\|\right)^2\\ &+\sum_{p=1}^{P}\frac{\rho}{2}S_2(\tilde{\mathbf{v}}_p(t+1),(1-r)\alpha)\\ &\times\left(\sqrt{(1-r)\alpha}-\|\tilde{\mathbf{v}}_p(t+1)\|\right)^2\\ &+\sum_{s=1}^{S}\frac{\rho}{2}S_3(\tilde{\mathbf{w}}_s(t+1),\eta\alpha)\left(\sqrt{\eta\alpha}-\|\tilde{\mathbf{w}}_s(t+1)\|\right)^2\\ \text{s.t.}\quad & \alpha\in[\alpha_L,\alpha_U],\end{aligned}\tag{57}$$

which implies that the objective function in (46) is actually a piecewise function that depends on the values of the unit-step functions. It must be pointed out that among $S_1(\tilde{\mathbf{v}}_p(t+1),(1+r)\alpha)$ and $S_2(\tilde{\mathbf{v}}_p(t+1),(1-r)\alpha)$, at most one attains the value of 1. To solve (57), we select the reasonable turning points from $\{\frac{\|\tilde{\mathbf{v}}_p(t+1)\|^2}{1+r},\frac{\|\tilde{\mathbf{v}}_p(t+1)\|^2}{1-r},\frac{\|\tilde{\mathbf{w}}_s(t+1)\|^2}{\eta}\}$, which align with (α_L,α_U).

Denote $\{\alpha_1(t+1),\ldots,\alpha_K(t+1)\}$ as the selected turning points arranged in ascending order. Then, we can obtain $(K+1)$ subfunctions in $[\alpha_L,\alpha_1(t+1)]$, $[\alpha_1(t+1),\alpha_2(t+1)]$, …, $[\alpha_K(t+1),\alpha_U]$. For the kth segment, there are concrete values for the three unit-step functions because $\alpha\in[\alpha_{k-1}(t+1),\alpha_k(t+1)]$. Thus, when $\alpha\in[\alpha_{k-1}(t+1),\alpha_k(t+1)]$, the objective function in (57) has the form of:

$$A_k\alpha+B_k\sqrt{\alpha}+C_k,\quad k=1,\ldots,K+1,\tag{58}$$

where A_k, B_k and C_k are:

$$\begin{aligned}A_k=&1+\frac{\rho}{2}\sum_{p=1}^{P}S_1(\tilde{\mathbf{v}}_p(t+1),(1+r)\alpha)(1+r)\\ &+\frac{\rho}{2}\sum_{p=1}^{P}S_2(\tilde{\mathbf{v}}_p(t+1),(1-r)\alpha)(1-r)\\ &+\frac{\rho}{2}\sum_{s=1}^{S}S_3(\tilde{\mathbf{w}}_s(t+1),\eta\alpha)\eta,\end{aligned}\tag{59}$$

$$\begin{aligned}B_k=&-\rho\sum_{p=1}^{P}S_1(\tilde{\mathbf{v}}_p(t+1),(1+r)\alpha)\|\tilde{\mathbf{v}}_p(t+1)\|\sqrt{1+r}\\ &-\rho\sum_{p=1}^{P}S_2(\tilde{\mathbf{v}}_p(t+1),(1-r)\alpha)\|\tilde{\mathbf{v}}_p(t+1)\|\sqrt{1-r}\\ &-\rho\sum_{s=1}^{S}S_3(\tilde{\mathbf{w}}_s(t+1),\eta\alpha)\|\tilde{\mathbf{w}}_s(t+1)\|\sqrt{\eta},\end{aligned}\tag{60}$$

and

$$\begin{aligned}C_k=&\frac{\rho}{2}\sum_{p=1}^{P}S_1(\tilde{\mathbf{v}}_p(t+1),(1+r)\alpha)\|\tilde{\mathbf{v}}_p(t+1)\|^2\\ &+\frac{\rho}{2}\sum_{p=1}^{P}S_2(\tilde{\mathbf{v}}_p(t+1),(1-r)\alpha)\|\tilde{\mathbf{v}}_p(t+1)\|^2\\ &+\frac{\rho}{2}\sum_{s=1}^{S}S_3(\tilde{\mathbf{w}}_s(t+1),\eta\alpha)\|\tilde{\mathbf{w}}_s(t+1)\|^2.\end{aligned}\tag{61}$$

Therefore, for the kth segment, the optimal variable value is given in (62), as shown bottom of this page and the corresponding minimum value is provided in (63) at the bottom of this page.

By selecting the smallest one from all the $(K+1)$ minimal values of the segments, e.g., $W_i=\min\{W_1,\ldots,W_{K+1}\}$, we determine $\alpha(t+1)$ as:

$$\alpha(t+1)=\hat{\varepsilon}_i.\tag{64}$$

Once $\alpha(t+1)$ is obtained, $\mathbf{v}_p(t+1)$ and $\mathbf{w}_s(t+1)$ are given by (50) and (51), respectively.

3) Update $\boldsymbol{\lambda}_{1,p}$ and $\boldsymbol{\lambda}_{2,s}$ using:

$$\begin{aligned}\boldsymbol{\lambda}_{1,p}(t+1)=\boldsymbol{\lambda}_{1,p}(t)+\rho\left(\mathbf{v}_p(t+1)-\tilde{\mathbf{F}}_p\bar{\mathbf{x}}(t+1)\right),\\ p=1,\ldots,P,\end{aligned}\tag{65}$$

$$\hat{\varepsilon}_k=\begin{cases}\frac{B_k^2}{4A_k^2}, & -\frac{B_k}{2A_k}\in[\|\alpha_{k-1}(t+1)\|,\|\alpha_k(t+1)\|]\\ \alpha_k(t+1), & A_k+\frac{B_k}{2\sqrt{\alpha_{k-1}(t+1)}}<0,A_k+\frac{B_k}{2\sqrt{\alpha_k(t+1)}}<0\\ \alpha_{k-1}(t+1), & A_k+\frac{B_k}{2\sqrt{\alpha_{k-1}(t+1)}}>0,A_k+\frac{B_k}{2\sqrt{\alpha_k(t+1)}}>0\end{cases},\tag{62}$$

$$W_k=\begin{cases}C_k-\frac{B_k^2}{4A_k}, & -\frac{B_k}{2A_k}\in[\|\alpha_{k-1}(t+1)\|,\|\alpha_k(t+1)\|]\\ A_k\alpha_k(t+1)+B_k\sqrt{\alpha_k(t+1)}+C_k, & A_k+\frac{B_k}{2\sqrt{\alpha_{k-1}(t+1)}}<0,A_k+\frac{B_k}{2\sqrt{\alpha_k(t+1)}}<0\\ A_k\alpha_{k-1}(t+1)+B_k\sqrt{\alpha_{k-1}(t+1)}+C_k, & A_k+\frac{B_k}{2\sqrt{\alpha_{k-1}(t+1)}}>0,A_k+\frac{B_k}{2\sqrt{\alpha_k(t+1)}}>0\end{cases}.\tag{63}$$

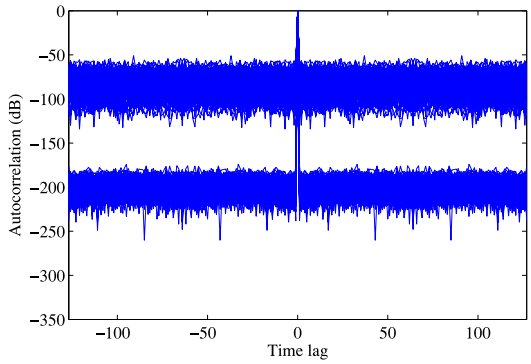

Fig. 1. Autocorrelations of periodic sequences by PeCAN in first test.

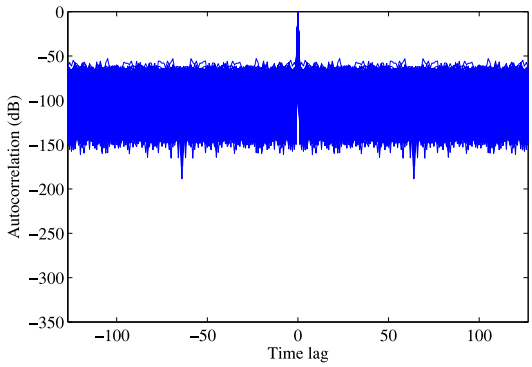

Fig. 2. Autocorrelations of periodic sequences by MISL in first test.

and

$$\boldsymbol{\lambda}_{2,s}(t+1) = \boldsymbol{\lambda}_{2,s}(t) + \rho\left(\mathbf{w}_s(t+1) - \hat{\mathbf{F}}_s\bar{\mathbf{x}}(t+1)\right), \quad s = 1, \ldots, S. \tag{66}$$

Steps 1) to 3) are repeated until a stopping criterion is reached.

V. Numerical Examples

In this section, we conduct computer simulations to assess the performance of the ADMM approach for unimodular sequence design. The first and second examples address the synthesis of the flat-spectrum periodic and aperiodic waveforms, respectively, whereas the third solves a more general spectral shaping problem.

A. Periodic Waveform Design With Flat Spectrum

We first consider generating a periodic unimodular sequence of period $N = 128$ with impulse-like autocorrelation function. In the ADMM algorithm, $\rho = 0.1$ is assigned and a maximum iteration number $T = 200\,000$ is employed as the stopping criterion. Comparison with the state-of-the-art methods, namely, PeCAN [11], MISL [13], and LPNN [14], is made. For all investigated schemes, a random phase (RP) sequence is used for initialization. With the use of 500 independent RP sequences, we produce a set of 500 designed waveforms for each method. The dB version of the normalized magnitude of $\tilde{r}_k$ in (2), that is, $20\log_{10}(|\tilde{r}_k|/N)$ is examined and the results of the PeCAN, MISL, LPNN and proposed algorithms are shown in Figs. 1 to4, respectively. From these autocorrelation functions, we compute

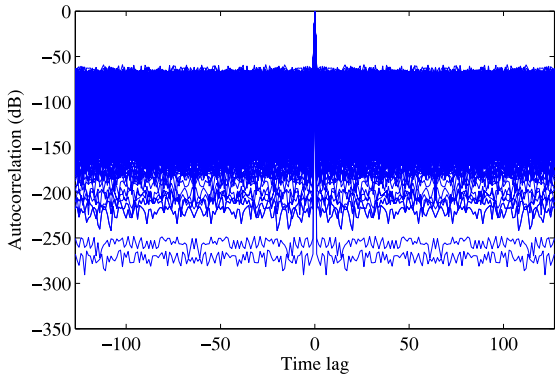

Fig. 3. Autocorrelations of periodic sequences by LPNN in first test.

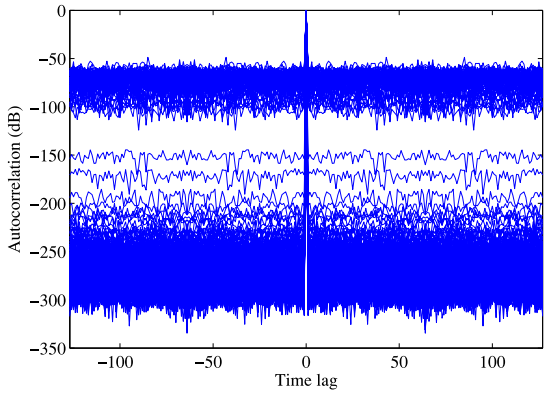

Fig. 4. Autocorrelations of periodic sequences by ADMM in first test.

the average and pick the one with minimum peak sidelobe for each method in Figs. 5 and 6, respectively. To further contrast the sidelobe attenuation performance, we tabulate the distributions of average and peak sidelobe levels of all 500 sequences where $\tilde{r}_0$ is removed, and list them in Table I. Moreover, the average runtimes of the four algorithms are provided in Table II.

We have also performed a preliminary study to examine the independence of the designed waveforms. The magnitude of the normalized cross-correlation is employed as the metric. For each investigated method, we choose the 10 best sequences, namely, those with minimum peak sidelobe levels. As cross-correlation measures the similarity between two sequences, there are 45 pairs and we pick the maximum cross-correlation for each pair. The results are plotted in Fig. 7 where we see that the maximum normalized cross-correlation is less than -10 dB, indicating that the designed sequences are highly independent for all four algorithms.

From Figs. 1 to 7 and Tables I to II, we obtain the findings as follows: (i) the sequences obtained from the ADMM method have minimum average autocorrelation sidelobe, namely, -253 dB. Most of the sidelobes, corresponding to 81.8%, have magnitudes less than -250 dB. Moreover, the peak sidelobe levels of most sequences, i.e., 73.8%, have magnitudes less than -250 dB. Among the four investigated schemes, the proposed one is the best because it provides the minimum autocorrelation sidelobe; (ii) In terms of complexity requirement, the MISL method is the most attractive, the ADMM and PeCAN are comparable, while the LPNN solution is extremely computationally demanding; (iii) as far as the peak sidelobe level is

TABLE I
COMPARISON OF SIDELOBE LEVEL DISTRIBUTIONS IN FIRST TEST WHERE LEFT COLUMN CORRESPONDS TO AVERAGE VALUE WHILE RIGHT COLUMN SHOWS THE PEAK

Method	≥ -50 dB	$(-50, -100]$ dB	$(-101, -150]$ dB	$(-150, -200]$ dB	$(-200, -250]$ dB	$(-250, -300]$ dB	< -300 dB
PeCAN	0, 1	214, 218	8, 3	121, 275	157, 3	0, 0	0, 0
MISL	0, 0	205, 252	295, 248	0, 0	0, 0	0, 0	0, 0
LPNN	0, 0	223, 259	223, 205	45, 30	7, 5	2, 1	0, 0
Proposed	0, 1	54, 54	1, 1	3, 4	23, 71	409, 369	0, 0

TABLE II
COMPARISON OF RUNTIMES IN FIRST TEST

Method	PeCAN	MISL	LPNN	Proposed
Runtime (s)	11.92	1.36	6893.41	13.27

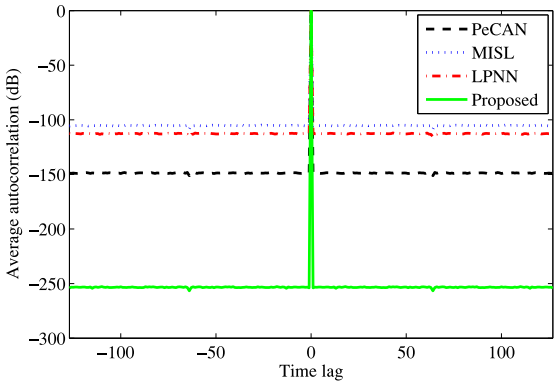

Fig. 5. Comparison of average autocorrelations in first test.

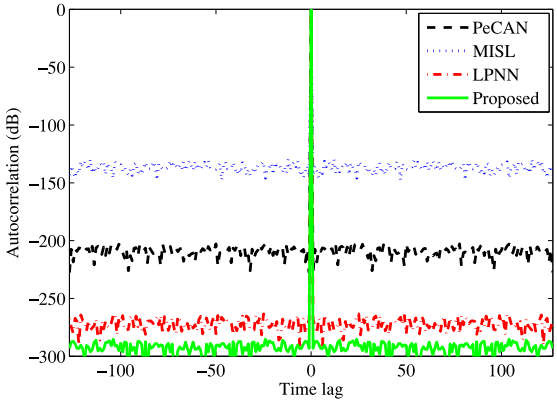

Fig. 6. Comparison of autocorrelations with lowest peak sidelobe levels in first test.

concerned, the proposed method produces the best sequence where its peak sidelobe level is less than -285 dB, as shown in Fig. 6; and (iv) From Fig. 7, the maximum cross-correlation of the ADMM algorithm is smallest among the other schemes, which is -12.19 dB. This implies that the designed sequences of the proposed method may have the highest independence.

B. Aperiodic Waveform Design With Flat Spectrum

In the second test, we design an aperiodic unimodular sequence of length $N = 128$. The ADMM algorithm in Section III is readily modified to achieve this task. The corresponding

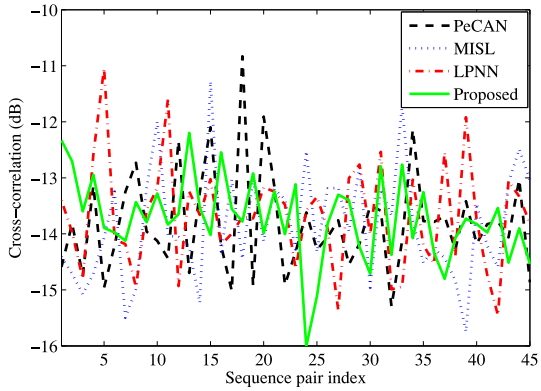

Fig. 7. Comparison of cross-correlations between sequences in first test.

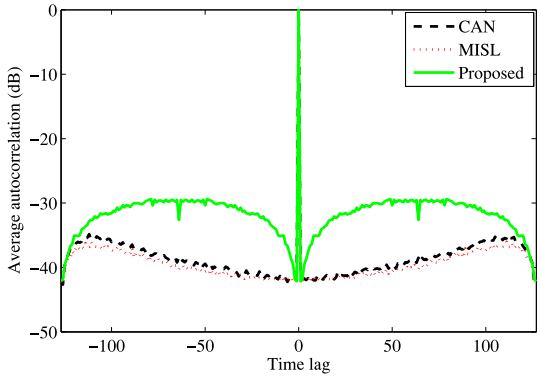

Fig. 8. Comparison of average autocorrelations in second test.

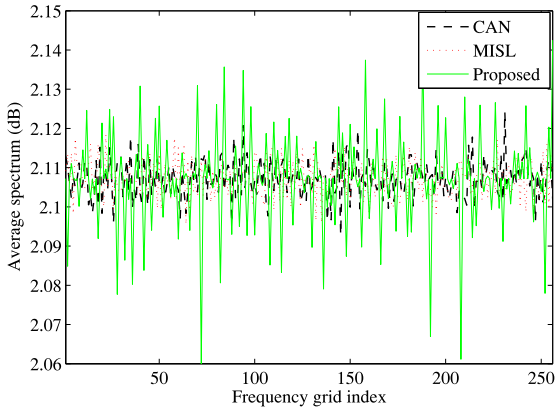

Fig. 9. Comparison of average spectra in second test.

competitive methods are CAN [10] and MISL [13], and their results are included in the comparison. The parameter settings are identical to those in the first experiment. The average aperiodic normalized autocorrelation in (3) based on 500 independent trials is plotted in Figs. 8 and 9 shows the mean spectra

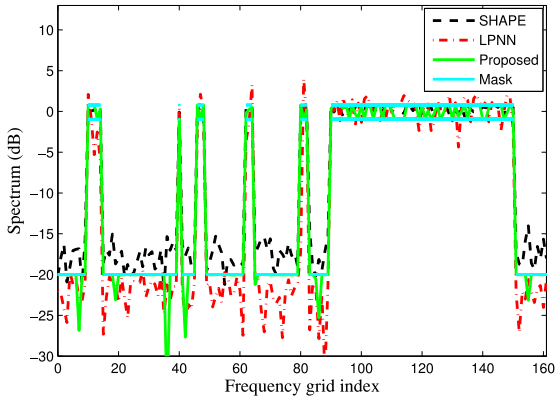

Fig. 10. Comparison of spectra in third test.

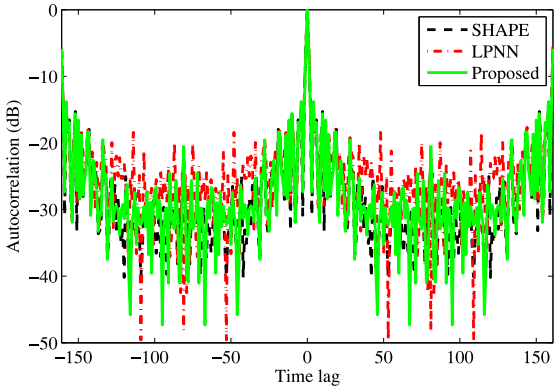

Fig. 11. Comparison of autocorrelations in third test.

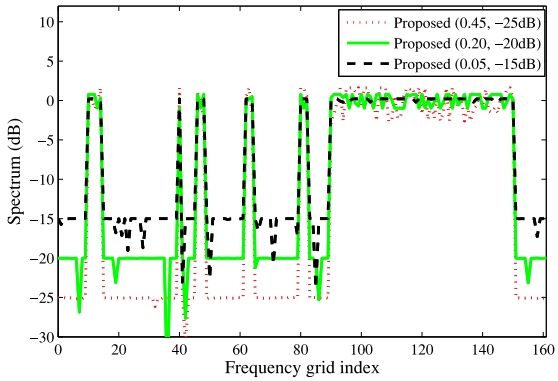

Fig. 12. Spectra with different r and η for proposed method.

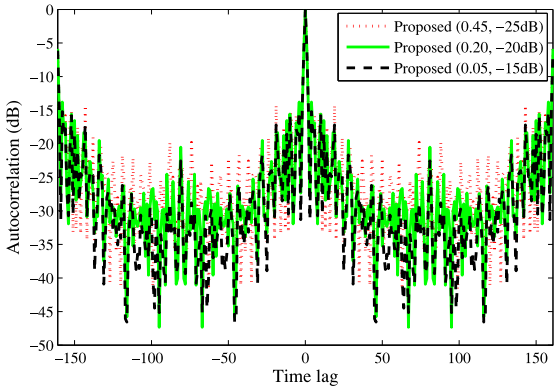

Fig. 13. Autocorrelation with different r and η for proposed method.

of the three methods. Besides, we select the sequence with the lowest peak sidelobe level for each of the proposed, MISL, and CAN methods, and their values are -23.93, -31.20, and -31.39 dB, respectively. We can observe that: (i) All solutions cannot provide a flat spectrum and their autocorrelation sidelobes are larger than those of the periodic case. This is because unlike the periodic autocorrelation, only N phase variables are used to deal with the flat-spectrum design with $2N$ frequency grids and thus fewer degrees of freedom are available in the aperiodic case; and (ii) In terms of autocorrelation sidelobes, ADMM, which is rigidly subject to the unimodular constraints on the sequence and auxiliary elements, is inferior to the CAN and MISL methods which have comparable performance.

C. Spectrally Constrained Waveform Design

Now we consider a radar application [35], where the overlayed and foreseen telecommunication systems spectrally coexist with it. The radar sampling rate is 810 kHz and pulse duration is 200 μs, which implies that the period of the periodic sequence is $N = 162$. The corresponding stopbands for the radar of interest are [0.0000,0.0617], [0.0988,0.2469], [0.2593,0.2840], [0.3086,0.3827], [0.4074,0.4938], [0.5185, 0.5556], and [0.9383,1.0000], and the rest correspond to the passbands available. In the proposed algorithm, we set $\rho = 0.1$, $T = 50\,000$, and the ripple and stopband levels are 0.2 and 0.01 or -20 dB, respectively, while the admissible range of α is [323,350]. The results of SHAPE [5], [12] and LPNN [14] methods are included for comparison purposes. Note that we do not consider the MISL algorithm because it cannot enforce a rigid spectral shape. The spectra and autocorrelations of the designed sequences are shown in Figs. 10 and 11, respectively. Our findings include: (i) the sequence obtained from the proposed method completely meets the required spectral constraints. On the other hand, the SHAPE scheme cannot control the stopband level well, while the LPNN algorithm requires properly designed weights [14] to attain low stopband level at the cost of large ripples; and (ii) All three methods have comparable autocorrelation sidelobes.

Finally, the effect of ripple and stopband levels of the ADMM method is studied. We consider three sets of ripple and sidelobe levels: $(r, \eta) = (0.05, -15\ \text{dB})$, $(0.2, -20\ \text{dB})$ and $(0.45, -25\ \text{dB})$. Fig. 12 shows the frequency spectra of the designed sequences and Fig. 13 plots the corresponding autocorrelations. We can see that: (i) the proposed algorithm can attain the ripple and sidelobe level constraints in all three cases; and (ii) In order to achieve a lower sidelobe level, a larger ripple will be required; (iii) The three different parameter configurations yield comparable sidelobe levels in their autocorrelations; and (iv) For all generated waveforms, their peak sidelobe level performance is poorer than that of the periodic and aperiodic cases at the expense of specified spectral requirement.

VI. Conclusion

In this paper, we have focused on the problem of unimodular and spectrally constrained waveform design via utilizing the ADMM algorithm. To design flat-spectrum waveform with unimodular constraint, we separate the objective function into

linear and quadratic components. By introducing auxiliary variables, the nonconvex unimodularity constraint is enforced on the linear term only but not on the quadratic counterpart, which facilitates the ADMM algorithm development. In designing spectrally constrained unimodular waveforms, we also introduce auxiliary variables to simplify the corresponding nonconvex optimization problem. Simulation results show that our proposed ADMM approach outperforms the state-of-the-art techniques for periodic unimodular waveform design with low sidelobe autocorrelation and arbitrary spectral shapes.

As a future work, we will focus on increasing the convergence rate of the proposed method. One possible solution is to adopt time-varying step size in the ADMM. Thorough examination on independence of the designed waveforms is also an interesting topic. Another research direction is to study waveform generation from the hardware realization point of view, including the temperature, mechanical structure, amplifier device, voltage generator, amplitude noise, phase noise, intermodulation factors, arbitrary waveform generators, and bits per sample.

APPENDIX A
FAST IMPLEMENTATION OF (32)

In this appendix, we present a fast implementation of (32) with the use of FFT. According to (14), we can construct the complex-valued version of (18) as:

$$\begin{aligned}
&\mathcal{L}_\rho^c(\mathbf{y},\mathbf{z},\boldsymbol{\lambda}_r,\boldsymbol{\lambda}_i)\\
&=\check{\mathbf{y}}^H\mathbf{A}_2^H\mathbf{A}_2\check{\mathbf{y}}+\check{\mathbf{z}}^H\mathbf{A}_2^H\mathbf{a}_1+\mathbf{a}_1^H\mathbf{A}_2\check{\mathbf{z}}\\
&\quad+\boldsymbol{\lambda}_r^T(\Re\{\check{\mathbf{y}}\}-\Re\{\check{\mathbf{z}}\})+\frac{\rho}{2}\|\Re\{\check{\mathbf{y}}\}-\Re\{\check{\mathbf{z}}\}\|^2\\
&\quad+\boldsymbol{\lambda}_i^T(\Im\{\check{\mathbf{y}}\}-\Im\{\check{\mathbf{z}}\})+\frac{\rho}{2}\|\Im\{\check{\mathbf{y}}\}-\Im\{\check{\mathbf{z}}\}\|^2, \qquad (67)
\end{aligned}$$

where $\boldsymbol{\lambda}_r\in\mathbb{R}^{(2N-1)\times 1}$ and $\boldsymbol{\lambda}_i\in\mathbb{R}^{(2N-1)\times 1}$ are the first and last halves of $\boldsymbol{\lambda}$ in (18), respectively.

According to $\bar{\mathbf{y}}=\left[(\Re\{\check{\mathbf{y}}\})^T\ (\Im\{\check{\mathbf{y}}\})^T\right]^T$ and (67), the complex-valued version of $\bar{\mathbf{y}}(t+1)$ in (32) can be determined from:

$$\begin{aligned}
\check{\mathbf{y}}(t+1)&=\arg\min_{\check{\mathbf{y}}}\ \check{\mathbf{y}}^H\mathbf{A}_2^H\mathbf{A}_2\check{\mathbf{y}}+\frac{\rho}{2}\left\|\check{\mathbf{y}}-\check{\mathbf{z}}+\frac{\boldsymbol{\lambda}^c}{\rho}\right\|^2\\
&=\arg\min_{\check{\mathbf{y}}}\ \check{\mathbf{y}}^H\mathbf{G}\check{\mathbf{y}}+\check{\mathbf{d}}^H(t+1)\check{\mathbf{y}}+\check{\mathbf{y}}^H\check{\mathbf{d}}(t+1)\\
&=-\mathbf{G}^{-1}\check{\mathbf{d}}(t+1), \qquad (68)
\end{aligned}$$

where

$$\mathbf{G}=\mathbf{A}_2^H\mathbf{A}_2+\frac{\rho}{2}\mathbf{I}_{2N-1}, \qquad (69)$$

$$\boldsymbol{\lambda}^c=\boldsymbol{\lambda}_r+\sqrt{-1}\boldsymbol{\lambda}_i, \qquad (70)$$

$$\begin{aligned}
\check{\mathbf{d}}(t+1)&=\frac{1}{2}\left(\boldsymbol{\lambda}^c(t)-\rho\check{\mathbf{z}}(t+1)\right),\\
&=\mathbf{d}_1(t+1)+\sqrt{-1}\mathbf{d}_2(t+1). \qquad (71)
\end{aligned}$$

In (71), $\mathbf{d}_1(t+1)\in\mathbb{R}^{(2N-1)\times 1}$ and $\mathbf{d}_2\in\mathbb{R}^{(2N-1)\times 1}$ are the first $(2N-1)$ and last $(2N-1)$ elements of $\mathbf{d}(t+1)$ defined in (31), i.e., $\mathbf{d}(t+1)=[\mathbf{d}_1^T(t+1)\ \mathbf{d}_2^T(t+1)]^T$.

Let $\mathbf{F}_1\in\mathbb{C}^{N\times(N-1)}$ be $\mathbf{F}$ with the first column removed and noting that $\mathbf{F}_1^H\mathbf{F}_1=N\mathbf{I}_{N-1}$, we have:

$$\begin{aligned}
\mathbf{G}&=\begin{bmatrix}\mathbf{F}_1 & -\sqrt{N}\mathbf{I}_N\end{bmatrix}^H\begin{bmatrix}\mathbf{F}_1 & -\sqrt{N}\mathbf{I}_N\end{bmatrix}+\frac{\rho}{2}\mathbf{I}_{2N-1},\\
&=\begin{bmatrix}\mathbf{F}_1^H\mathbf{F}_1 & -\sqrt{N}\mathbf{F}_1^H\\ -\sqrt{N}\mathbf{F}_1 & N\mathbf{I}_N\end{bmatrix}+\frac{\rho}{2}\mathbf{I}_{2N-1},\\
&=\begin{bmatrix}(N+\frac{\rho}{2})\mathbf{I}_{N-1} & -\sqrt{N}\mathbf{F}_1^H\\ -\sqrt{N}\mathbf{F}_1 & (N+\frac{\rho}{2})\mathbf{I}_N\end{bmatrix}, \qquad (72)
\end{aligned}$$

According to the block matrix inversion lemma [30], [31], the inverse of $\mathbf{G}$ can be written in the form of (73) shown in the bottom of this page. With the use of

$$\mathbf{F}\mathbf{F}^H=\mathbf{1}_N\mathbf{1}_N^T+\mathbf{F}_1\mathbf{F}_1^H=N\mathbf{I}_N, \qquad (74)$$

and

$$\begin{aligned}
\mathbf{F}_1^H\left(\mathbf{1}_N\mathbf{1}_N^T\right)&=\mathbf{F}_1^H\left(N\mathbf{I}_N-\mathbf{F}_1\mathbf{F}_1^H\right)\\
&=N\mathbf{F}_1^H-\mathbf{F}_1^H\mathbf{F}_1\mathbf{F}_1^H\\
&=N\mathbf{F}_1^H-N\mathbf{I}_{N-1}\mathbf{F}_1^H=\mathbf{0}_{N-1}, \qquad (75)
\end{aligned}$$

and applying the matrix inversion lemma, we obtain:

$$\begin{aligned}
&\left(\frac{4N\rho+\rho^2}{4N+2\rho}\mathbf{I}_N+\frac{2N}{2N+\rho}\mathbf{1}_N\mathbf{1}_N^T\right)^{-1}\\
&=\left(\frac{4N\rho+\rho^2}{4N+2\rho}\mathbf{I}_N\right)^{-1}\\
&\quad-\frac{\frac{2N}{2N+\rho}\left(\frac{4N\rho+\rho^2}{4N+2\rho}\mathbf{I}_N\right)^{-1}\mathbf{1}_N\mathbf{1}_N^T\left(\frac{4N\rho+\rho^2}{4N+2\rho}\mathbf{I}_N\right)^{-1}}{1+\frac{2N}{2N+\rho}\mathbf{1}_N^T\left(\frac{4N\rho+\rho^2}{4N+2\rho}\mathbf{I}_N\right)^{-1}\mathbf{1}_N}\\
&=\frac{4N+2\rho}{4N\rho+\rho^2}\mathbf{I}_N-\frac{8N}{(2N+\rho)(4N\rho+\rho^2)}\mathbf{1}_N\mathbf{1}_N^T \qquad (76)
\end{aligned}$$

$$\begin{aligned}
\mathbf{G}^{-1}&=\begin{bmatrix}\left((N+\frac{\rho}{2})\mathbf{I}_{N-1}-\frac{N}{N+\frac{\rho}{2}}\mathbf{F}_1^H\mathbf{F}_1\right)^{-1} & \frac{\sqrt{N}}{N+\frac{\rho}{2}}\mathbf{F}_1^H\left((N+\frac{\rho}{2})\mathbf{I}_N-\frac{N}{N+\frac{\rho}{2}}\mathbf{F}_1\mathbf{F}_1^H\right)^{-1}\\ \frac{\sqrt{N}}{N+\frac{\rho}{2}}\mathbf{F}_1\left((N+\frac{\rho}{2})\mathbf{I}_{N-1}-\frac{N}{N+\frac{\rho}{2}}\mathbf{F}_1^H\mathbf{F}_1\right)^{-1} & \left((N+\frac{\rho}{2})\mathbf{I}_N-\frac{N}{N+\frac{\rho}{2}}\mathbf{F}_1\mathbf{F}_1^H\right)^{-1}\end{bmatrix}\\
&=\begin{bmatrix}\frac{4N+2\rho}{4N\rho+\rho^2}\mathbf{I}_{N-1} & \frac{\sqrt{N}}{N+\frac{\rho}{2}}\mathbf{F}_1^H\left(\frac{4N\rho+\rho^2}{4N+2\rho}\mathbf{I}_N+\frac{2N}{2N+\rho}\mathbf{1}_N\mathbf{1}_N^T\right)^{-1}\\ \frac{4\sqrt{N}}{4N\rho+\rho^2}\mathbf{F}_1 & \left(\frac{4N\rho+\rho^2}{4N+2\rho}\mathbf{I}_N+\frac{2N}{2N+\rho}\mathbf{1}_N\mathbf{1}_N^T\right)^{-1}\end{bmatrix}. \qquad (73)
\end{aligned}$$

and

$$\begin{aligned}&\frac{\sqrt{N}}{N+\frac{\rho}{2}}\mathbf{F}_1^H\left(\frac{4N\rho+\rho^2}{4N+2\rho}\mathbf{I}_N+\frac{2N}{2N+\rho}\mathbf{1}_N\mathbf{1}_N^T\right)^{-1}\\&=\frac{\sqrt{N}}{N+\frac{\rho}{2}}\mathbf{F}_1^H\\&\times\left(\frac{4N+2\rho}{4N\rho+\rho^2}\mathbf{I}_N-\frac{8N}{(2N+\rho)(4N\rho+\rho^2)}\mathbf{1}_N\mathbf{1}_N^T\right)\\&=\frac{4\sqrt{N}}{4N\rho+\rho^2}\mathbf{F}_1^H.\end{aligned}\tag{77}$$

Therefore, $\mathbf{G}^{-1}$ can be simplified as (78), as shown on the bottom of this page. Moreover, we partition $\check{\mathbf{d}}(t+1)$ into:

$$\check{\mathbf{d}}(t+1)=\begin{bmatrix}\mathbf{d}_3(t+1)\\\mathbf{d}_4(t+1)\end{bmatrix},\tag{79}$$

where $\mathbf{d}_3(t+1)$ and $\mathbf{d}_4(t+1)$ consist of the first $(N-1)$ and last N elements of $\check{\mathbf{d}}(t+1)$, respectively. Therefore, $-\mathbf{G}^{-1}\check{\mathbf{d}}(t+1)$ can be calculated according to (80) on the bottom of this page. After determining $\check{\mathbf{y}}(t+1)$, $\bar{\mathbf{y}}(t+1)$ is then obtained from $\check{\mathbf{y}}(t+1)$ based on the definition of $\bar{\mathbf{y}}$.

Note that

$$\begin{aligned}\mathbf{F}^H\mathbf{d}_4(t+1)&=\begin{bmatrix}\mathbf{1}_N & \mathbf{F}_1\end{bmatrix}^H\mathbf{d}_4(t+1)=\begin{bmatrix}\mathbf{1}_N^T\\\mathbf{F}_1^H\end{bmatrix}\mathbf{d}_4(t+1)\\&=\begin{bmatrix}\mathbf{1}_N^T\mathbf{d}_4(t+1)\\\mathbf{F}_1^H\mathbf{d}_4(t+1)\end{bmatrix}.\end{aligned}\tag{81}$$

That is, $\mathbf{F}_1^H\mathbf{d}_4(t+1)$ is equal to $\mathbf{F}^H\mathbf{d}_4(t+1)$ with the first element removed. Therefore, we can apply the inverse FFT [32] on $\mathbf{d}_4(t+1)$ and then discard the first element to obtain $\mathbf{F}_1^H\mathbf{d}_4(t+1)$. On the other hand, we write

$$\mathbf{F}_1\mathbf{d}_3(t+1)=\begin{bmatrix}\mathbf{1}_N & \mathbf{F}_1\end{bmatrix}\begin{bmatrix}0\\\mathbf{d}_3(t+1)\end{bmatrix}=\mathbf{F}\begin{bmatrix}0\\\mathbf{d}_3(t+1)\end{bmatrix}\tag{82}$$

so that $\mathbf{F}_1\mathbf{d}_3(t+1)$ can be obtained from the FFT of $[0\,\mathbf{d}_3^T(t+1)]^T$. Both $\mathbf{F}_1^H\mathbf{d}_4(t+1)$ and $\mathbf{F}_1\mathbf{d}_3(t+1)$ have a complexity order of $N\log N$ [32]–[34]. Additionally, $\frac{4N+2\rho}{4N\rho+\rho^2}\mathbf{d}_3(t+1)$, $\frac{4\sqrt{N}}{4N\rho+\rho^2}\times\left(\mathbf{F}_1^H\mathbf{d}_4(t+1)\right)$, $\frac{4N+2\rho}{4N\rho+\rho^2}\mathbf{d}_4(t+1)$, $\frac{4\sqrt{N}}{4N\rho+\rho^2}\times(\mathbf{F}_1\mathbf{d}_3(t+1))$ and $\frac{8N}{(2N+\rho)(4N\rho+\rho^2)}\mathbf{1}_N\times(\mathbf{1}_N^T\mathbf{d}_4(t+1))$ need $(4N-1)$ multiplications in total. Therefore, the update of $\bar{\mathbf{y}}(t+1)$ from $-\mathbf{G}^{-1}\check{\mathbf{d}}(t+1)$ has a complexity of $\mathcal{O}(N\log N)$, which is lower than $\mathcal{O}\left(N^2\right)$ required in (32).

Similarly, the matrix inversion lemma and FFT operations can be applied to aperiodic flat-spectrum waveform design to accelerate the corresponding implementation.

Appendix B
Convergence Analysis

We now apply the results in [21], [22], [24] to study the local convergence of the proposed ADMM algorithm.

Lemma 2: The objective function of (15) satisfies: (i) its two components, namely, $\bar{\mathbf{y}}^T\mathbf{H}\bar{\mathbf{y}}$ and $2\mathbf{c}^T\bar{\mathbf{z}}$, are closed, proper, and convex; and (ii) the unaugmented Lagrangian $\mathcal{L}_0(\bar{\mathbf{y}},\bar{\mathbf{z}},\boldsymbol{\lambda})$ for (15) has a saddle point $(\bar{\mathbf{y}}^\star,\bar{\mathbf{z}}^\star,\boldsymbol{\lambda}^\star)$. Let $q(t+1)=\bar{\mathbf{y}}^T(t+1)\mathbf{H}\bar{\mathbf{y}}(t+1)+2\mathbf{c}^T\bar{\mathbf{z}}(t+1)$. Then the following inequality holds:

$$q^\star\le q(t+1)+{\boldsymbol{\lambda}^\star}^T\mathbf{r}(t+1),\tag{83}$$

where the residual $\mathbf{r}(t+1)$ at the $(t+1)$th iteration is defined as:

$$\mathbf{r}(t+1)=\bar{\mathbf{y}}(t+1)-\bar{\mathbf{z}}(t+1).\tag{84}$$

Proof: Since $(\bar{\mathbf{y}}^\star,\bar{\mathbf{z}}^\star,\boldsymbol{\lambda}^\star)$ is a saddle point, we have:

$$\mathcal{L}_0\left(\bar{\mathbf{y}}^\star,\bar{\mathbf{z}}^\star,\boldsymbol{\lambda}^\star\right)\le\mathcal{L}_0\left(\bar{\mathbf{y}}(t+1),\bar{\mathbf{z}}(t+1),\boldsymbol{\lambda}^\star\right).\tag{85}$$

At the equilibrium point $(\bar{\mathbf{y}}^\star,\bar{\mathbf{z}}^\star,\boldsymbol{\lambda}^\star)$, we have $\bar{\mathbf{y}}^\star-\bar{\mathbf{z}}^\star=\mathbf{0}_{4N-2}$ and $\mathcal{L}_0\left(\bar{\mathbf{y}}^\star,\bar{\mathbf{z}}^\star,\boldsymbol{\lambda}^\star\right)=q^\star$. Substituting $q^\star$ and $q(t+1)$ into (85) yields (83). The proof is complete. ■

Lemma 3: The following inequality holds:

$$\begin{aligned}q(t+1)-q^\star\le&-\boldsymbol{\lambda}^T(t+1)\mathbf{r}(t+1)\\&-\rho\left(\bar{\mathbf{y}}(t+1)-\bar{\mathbf{y}}(t)\right)^T\left(-r(t+1)+\bar{\mathbf{y}}(t+1)-\bar{\mathbf{y}}^\star\right).\end{aligned}\tag{86}$$

Proof: Since

$$\bar{\mathbf{y}}(t+1)=\arg\min_{\bar{\mathbf{y}}}\mathcal{L}_\rho\left(\bar{\mathbf{y}},\bar{\mathbf{z}}(t+1),\boldsymbol{\lambda}(t)\right),\tag{87}$$

we have

$$\begin{aligned}&0\in\partial L_\rho\left(\bar{\mathbf{y}}(t+1),\bar{\mathbf{z}}(t+1),\boldsymbol{\lambda}(t)\right)\\&=2\mathbf{H}\bar{\mathbf{y}}(t+1)+\boldsymbol{\lambda}(t)+\rho\left(\bar{\mathbf{y}}(t+1)-\bar{\mathbf{z}}(t+1)\right).\end{aligned}\tag{88}$$

Furthermore, inserting $\boldsymbol{\lambda}(t+1)=\boldsymbol{\lambda}(t)+\rho\mathbf{r}(t+1)$ into (88) yields:

$$0\in2\mathbf{H}\bar{\mathbf{y}}(t+1)+\boldsymbol{\lambda}(t+1),\tag{89}$$

which is equivalent to the following optimization problem:

$$\bar{\mathbf{y}}(t+1)=\arg\min_{\bar{\mathbf{y}}}\quad\bar{\mathbf{y}}^T\mathbf{H}\bar{\mathbf{y}}+\boldsymbol{\lambda}^T(t+1)\bar{\mathbf{y}}.\tag{90}$$

$$\mathbf{G}^{-1}=\begin{bmatrix}\frac{4N+2\rho}{4N\rho+\rho^2}\mathbf{I}_{N-1} & \frac{4\sqrt{N}}{4N\rho+\rho^2}\mathbf{F}_1^H\\\frac{4\sqrt{N}}{4N\rho+\rho^2}\mathbf{F}_1 & \frac{4N+2\rho}{4N\rho+\rho^2}\mathbf{I}_N-\frac{8N}{(2N+\rho)(4N\rho+\rho^2)}\mathbf{1}_N\mathbf{1}_N^T\end{bmatrix}.\tag{78}$$

$$\mathbf{G}^{-1}\check{\mathbf{d}}(t+1)=-\begin{bmatrix}\frac{4N+2\rho}{4N\rho+\rho^2}\mathbf{d}_3(t+1)+\frac{4\sqrt{N}}{4N\rho+\rho^2}\mathbf{F}_1^H\mathbf{d}_4(t+1)\\\frac{4\sqrt{N}}{4N\rho+\rho^2}\mathbf{F}_1\mathbf{d}_3(t+1)+\frac{4N+2\rho}{4N\rho+\rho^2}\mathbf{d}_4(t+1)-\frac{8N}{(2N+\rho)(4N\rho+\rho^2)}\mathbf{1}_N\times(\mathbf{1}_N^T\mathbf{d}_4(t+1))\end{bmatrix}.\tag{80}$$

At the $(t+1)$th iteration, the update of $\boldsymbol{\lambda}(t+1)$ is given as $\boldsymbol{\lambda}(t+1)=\boldsymbol{\lambda}(t)+\rho\left(\bar{\mathbf{y}}(t+1)-\bar{\mathbf{z}}(t+1)\right)$. Hence, we have: $\boldsymbol{\lambda}(t)=\boldsymbol{\lambda}(t+1)-\rho\left(\bar{\mathbf{y}}(t+1)-\bar{\mathbf{z}}(t+1)\right)$. Replacing $\boldsymbol{\lambda}(t)$ in

$$\begin{aligned}\bar{\mathbf{z}}(t+1)&=\arg\min_{\bar{\mathbf{z}}} L_\rho\left(\bar{\mathbf{y}}(t),\bar{\mathbf{z}},\boldsymbol{\lambda}(t)\right)\\&=\arg\min_{\bar{\mathbf{z}}} 2\mathbf{c}^T\bar{\mathbf{z}}-\boldsymbol{\lambda}^T(t)\bar{\mathbf{z}}-\rho\bar{\mathbf{y}}^T(t)\bar{\mathbf{z}}\\&\text{s.t.}\qquad |z_n|=1,\quad n=1,\ldots,2N-1,\end{aligned}\tag{91}$$

with $\boldsymbol{\lambda}(t)=\boldsymbol{\lambda}(t+1)-\rho\left(\bar{\mathbf{y}}(t+1)-\bar{\mathbf{z}}(t+1)\right)$, we have:

$$\begin{aligned}&\bar{\mathbf{z}}(t+1)\\&=\arg\min_{\bar{\mathbf{z}}} 2\mathbf{c}^T\bar{\mathbf{z}}-\left(\boldsymbol{\lambda}(t+1)-\rho(\bar{\mathbf{y}}(t+1)-\bar{\mathbf{y}}(t))\right)^T\bar{\mathbf{z}}\\&\text{s.t.}\qquad |z_n|=1,\quad n=1,\ldots,2N-1.\end{aligned}\tag{92}$$

According to (90) and (92), we have:

$$\begin{aligned}&\bar{\mathbf{y}}^T(t+1)\mathbf{H}\bar{\mathbf{y}}(t+1)+\boldsymbol{\lambda}^T(t+1)\bar{\mathbf{y}}(t+1)\\&\quad\le\bar{\mathbf{y}}^{\star T}\mathbf{H}\bar{\mathbf{y}}^\star+\boldsymbol{\lambda}^T(t+1)\bar{\mathbf{y}}^\star,\end{aligned}\tag{93}$$

and

$$\begin{aligned}&2\mathbf{c}^T\bar{\mathbf{z}}(t+1)-\left(\boldsymbol{\lambda}(t+1)-\rho(\bar{\mathbf{y}}(t+1)-\bar{\mathbf{y}}(t))\right)^T\bar{\mathbf{z}}(t+1)\\&\quad\le 2\mathbf{c}^T\bar{\mathbf{z}}^\star-\left(\boldsymbol{\lambda}(t+1)-\rho(\bar{\mathbf{y}}(t+1)-\bar{\mathbf{y}}(t))\right)^T\bar{\mathbf{z}}^\star.\end{aligned}\tag{94}$$

Adding (93) and (94), and employing $\bar{\mathbf{y}}^\star-\bar{\mathbf{z}}^\star=\mathbf{0}_{4N-2}$, we obtain:

$$\begin{aligned}&\bar{\mathbf{y}}^T(t+1)\mathbf{H}\bar{\mathbf{y}}(t+1)+\boldsymbol{\lambda}^T(t+1)\bar{\mathbf{y}}(t+1)\\&+2\mathbf{c}^T\bar{\mathbf{z}}(t+1)-\left(\boldsymbol{\lambda}(t+1)-\rho(\bar{\mathbf{y}}(t+1)-\bar{\mathbf{y}}(t))\right)^T\bar{\mathbf{z}}(t+1)\\&\le\bar{\mathbf{y}}^{\star T}\mathbf{H}\bar{\mathbf{y}}^\star+\boldsymbol{\lambda}^T(t+1)\bar{\mathbf{y}}^\star\\&+2\mathbf{c}^T\bar{\mathbf{z}}^\star-\left(\boldsymbol{\lambda}(t+1)-\rho(\bar{\mathbf{y}}(t+1)-\bar{\mathbf{y}}(t))\right)^T\bar{\mathbf{z}}^\star\\&\Longrightarrow q(t+1)-q^\star\le-\boldsymbol{\lambda}^T(t+1)\mathbf{r}(t+1)\\&-\rho\left(\bar{\mathbf{y}}(t+1)-\bar{\mathbf{y}}(t)\right)^T\left(-r(t+1)+\bar{\mathbf{y}}(t+1)-\bar{\mathbf{y}}^\star\right),\end{aligned}\tag{95}$$

where $\bar{\mathbf{z}}^\star=\bar{\mathbf{y}}^\star$ and $\mathbf{r}(t+1)=\bar{\mathbf{y}}(t+1)-\bar{\mathbf{z}}(t+1)$ are applied. The proof is complete. ■

Lemma 4: Let $(\bar{\mathbf{y}}^\star,\bar{\mathbf{z}}^\star,\boldsymbol{\lambda}^\star)$ be a saddle point for $\mathcal{L}_0(\bar{\mathbf{y}},\bar{\mathbf{z}},\boldsymbol{\lambda})$. Define the Lyapunov function:

$$V(t)=\frac{1}{\rho}\|\boldsymbol{\lambda}(t)-\boldsymbol{\lambda}^\star\|^2+\rho\|\bar{\mathbf{y}}(t)-\bar{\mathbf{y}}^\star\|^2.\tag{96}$$

Then, the following inequality holds:

$$V(t+1)\le V(t)-\rho\|\mathbf{r}(t+1)\|^2-\rho\|\bar{\mathbf{y}}(t+1)-\bar{\mathbf{y}}(t)\|^2.\tag{97}$$

Proof: Adding (83) and (86) together results in:

$$\begin{aligned}&2\left(\boldsymbol{\lambda}(t+1)-\boldsymbol{\lambda}^\star\right)^T\mathbf{r}(t+1)-2\rho\left(\bar{\mathbf{y}}(t+1)-\bar{\mathbf{y}}(t)\right)^T\mathbf{r}(t+1)\\&+2\rho\left(\bar{\mathbf{y}}(t+1)-\bar{\mathbf{y}}(t)\right)^T\left(\bar{\mathbf{y}}(t+1)-\bar{\mathbf{y}}^\star\right)\le 0.\end{aligned}\tag{98}$$

Substituting $\boldsymbol{\lambda}(t+1)=\boldsymbol{\lambda}(t)+\rho\mathbf{r}(t+1)$ into $2\left(\boldsymbol{\lambda}(t+1)-\boldsymbol{\lambda}^\star\right)^T\mathbf{r}(t+1)$ in (98) yields:

$$\begin{aligned}&2\left(\boldsymbol{\lambda}(t)+\rho\mathbf{r}(t+1)-\boldsymbol{\lambda}^\star\right)^T\mathbf{r}(t+1)\\&=2\left(\boldsymbol{\lambda}(t)-\boldsymbol{\lambda}^\star\right)^T\mathbf{r}(t+1)+\rho\|\mathbf{r}(t+1)\|_2^2+\rho\|\mathbf{r}(t+1)\|^2.\end{aligned}\tag{99}$$

Then, putting $\mathbf{r}(t+1)=\frac{1}{\rho}(\boldsymbol{\lambda}(t+1)-\boldsymbol{\lambda}(t))$ into $2\left(\boldsymbol{\lambda}(t)-\boldsymbol{\lambda}^\star\right)^T\mathbf{r}(t+1)+\rho\|\mathbf{r}(t+1)\|^2$ in (99), we obtain:

$$\begin{aligned}&\frac{2}{\rho}\left(\boldsymbol{\lambda}(t)-\boldsymbol{\lambda}^\star\right)^T\left(\boldsymbol{\lambda}(t+1)-\boldsymbol{\lambda}(t)\right)+\frac{1}{\rho}\|\boldsymbol{\lambda}(t+1)-\boldsymbol{\lambda}(t)\|^2\\&=\frac{1}{\rho}\|\boldsymbol{\lambda}(t+1)-\boldsymbol{\lambda}^\star\|^2-\frac{1}{\rho}\|\boldsymbol{\lambda}(t)-\boldsymbol{\lambda}^\star\|^2.\end{aligned}\tag{100}$$

Additionally,

$$\begin{aligned}&\rho\|\mathbf{r}(t+1)\|^2-2\rho\left(\bar{\mathbf{y}}(t+1)-\bar{\mathbf{y}}(t)\right)^T\mathbf{r}(t+1)\\&+2\rho\left(\bar{\mathbf{y}}(t+1)-\bar{\mathbf{y}}(t)\right)^T\left(\bar{\mathbf{y}}(t+1)-\bar{\mathbf{y}}^\star\right)\\&=\rho\|\mathbf{r}(t+1)-\bar{\mathbf{y}}(t+1)+\bar{\mathbf{y}}(t)\|^2+\rho\|\bar{\mathbf{y}}(t+1)-\bar{\mathbf{y}}^\star\|^2\\&\quad-\rho\|\bar{\mathbf{y}}(t)-\bar{\mathbf{y}}^\star\|^2.\end{aligned}\tag{101}$$

Combining (100) and (101), we rewrite (98) as:

$$\begin{aligned}&\frac{1}{\rho}\|\boldsymbol{\lambda}(t+1)-\boldsymbol{\lambda}^\star\|^2-\frac{1}{\rho}\|\boldsymbol{\lambda}(t)-\boldsymbol{\lambda}^\star\|^2\\&+\rho\|\mathbf{r}(t+1)-\bar{\mathbf{y}}(t+1)+\bar{\mathbf{y}}(t)\|^2\\&+\rho\|\bar{\mathbf{y}}(t+1)-\bar{\mathbf{y}}^\star\|^2-\rho\|\bar{\mathbf{y}}(t)-\bar{\mathbf{y}}^\star\|^2\le 0.\end{aligned}\tag{102}$$

According to (90), we have:

$$\begin{aligned}&\bar{\mathbf{y}}^T(t+1)\mathbf{H}\bar{\mathbf{y}}(t+1)+\boldsymbol{\lambda}^T(t+1)\bar{\mathbf{y}}(t+1)\\&\quad\le\bar{\mathbf{y}}^T(t)\mathbf{H}\bar{\mathbf{y}}(t)+\boldsymbol{\lambda}^T(t+1)\bar{\mathbf{y}}(t),\end{aligned}\tag{103}$$

and

$$\begin{aligned}&\bar{\mathbf{y}}^T(t)\mathbf{H}\bar{\mathbf{y}}(t)+\boldsymbol{\lambda}^T(t)\bar{\mathbf{y}}(t)\\&\quad\le\bar{\mathbf{y}}^T(t+1)\mathbf{H}\bar{\mathbf{y}}(t+1)+\boldsymbol{\lambda}^T(t)\bar{\mathbf{y}}(t+1).\end{aligned}\tag{104}$$

Adding (103) and (104) yields:

$$\begin{aligned}&\boldsymbol{\lambda}^T(t+1)\bar{\mathbf{y}}(t+1)+\boldsymbol{\lambda}^T(t)\bar{\mathbf{y}}(t)\\&\le\boldsymbol{\lambda}^T(t+1)\bar{\mathbf{y}}(t)+\boldsymbol{\lambda}^T(t)\bar{\mathbf{y}}(t+1)\\&\Rightarrow\mathbf{r}(t+1)^T\left(\bar{\mathbf{y}}(t+1)-\bar{\mathbf{y}}(t)\right)\le 0.\end{aligned}\tag{105}$$

Based on the Lyapunov function defined in (96), we rewrite (102) as:

$$\begin{aligned}&V(t+1)-V(t)+\rho\|\mathbf{r}(t+1)-\bar{\mathbf{y}}(t+1)+\bar{\mathbf{y}}(t)\|^2\le 0\\&\Rightarrow V(t+1)-V(t)+\rho\|\mathbf{r}(t+1)\|^2+\rho\|\bar{\mathbf{y}}(t+1)-\bar{\mathbf{y}}(t)\|^2\\&-2\rho\mathbf{r}(t+1)^T\left(\bar{\mathbf{y}}(t+1)-\bar{\mathbf{y}}(t)\right)\le 0.\end{aligned}\tag{106}$$

Combining (105) and (106) gives (97). The proof is complete. ■

From (97), we can see that V_k decreases in each iteration by an amount which is related to the norm of primal residual $\mathbf{r}(t+1)$ and on the change of $\bar{\mathbf{y}}(t)$ over one iteration [21], [22],

[24]. Furthermore, $V_k \leq V_0$ indicates that both $\boldsymbol{\lambda}$ and $\bar{\mathbf{y}}(t)$ are bounded. From (89), we also have:

$$\sum_{t=1}^{\infty} \left(\rho\|\mathbf{r}(t+1)\|^2 + \rho\|\bar{\mathbf{y}}(t+1) - \bar{\mathbf{y}}(t)\|^2\right) \leq V_0, \quad (107)$$

which implies that $\mathbf{r}(t+1) \to \mathbf{0}_{4N-2}$ and $\bar{\mathbf{y}}(t+1) - \bar{\mathbf{y}}(t) \to \mathbf{0}_{4N-2}$ as the iteration number $t \to \infty$.

From (86), it is observed that $\bar{\mathbf{z}}(t+1) - \bar{\mathbf{z}}^{\star}$ is bounded and both $\mathbf{r}(t+1)$ and $\bar{\mathbf{y}}(t+1) - \bar{\mathbf{y}}(t)$ approach zero [21], [22], [24]. Then, $q(t+1) - q^{\star}$ of (86) tends to zero as $t \to \infty$. Therefore, both (83) and (86) result in

$$\lim_{t\to\infty} q(t+1) = q^{\star}, \quad (108)$$

which is the desired objective convergence.

Based on the ADMM framework, we can obtain similar derivations for the aperiodic and spectrally constrained waveform design problems where the aforementioned convergence proof still holds true.

REFERENCES

[1] J. Li and P. Stoica, *MIMO Radar Signal Processing*. Hoboken, NJ, USA: Wiley, 2009.

[2] F. Gini, A. De Maio, and L. K. Patton, *Waveform Design and Diversity for Advanced Radar*. London, U.K.: Institution of Engineering and Technology, 2012.

[3] M. Wicks, E. Mokole, S. Blunt, and R. Schneible, Eds., *Principles of Waveform Diversity and Design*. Raleigh, NC, USA: SciTech Pub., 2011.

[4] H. He, J. Li, and P. Stoica. *Waveform Design for Active Sensing Systems: A Computational Approach*. Cambridge, U. K.: Cambridge Univ. Press, 2012.

[5] W. Rowe, P. Stoica, and J. Li, "Spectrally constrained waveform design," *IEEE Signal Process. Mag.*, vol. 157, no. 3, pp. 157–162, May 2014.

[6] A. B. MacKenzie and L. A. DaSilva, "Application of signal processing to addressing wireless data demand," *IEEE Signal Process. Mag.*, vol. 29, no. 6, pp. 168–166, Nov. 2012.

[7] H. Griffiths *et al.*, "Radar spectrum engineering and maganement: Technical and regulatory issues," *Proc. IEEE*, vol. 103, no. 1, pp. 85–102, Jan. 2015.

[8] A. Aubry, A. De Maio, M. Piezzo, and A. Farina, "Radar waveform design in a spectrally crowded environment via nonconvex quadratic optimization," *IEEE Trans. Aerosp. Electron. Syst.*, vol. 50, no. 2, pp. 1138–1152, Apr. 2014.

[9] A. Aubry, A. De Maio, Y. Huang, M. Piezzo, and A. Farina, "A new radar waveform design algorithm with improved feasibility for spectral coexistence," *IEEE Trans. Aerosp. Electron. Syst.*, vol. 51, no. 2, pp. 1029–1038, Apr. 2015.

[10] P. Stoica, H. He, and J. Li, "New algorithms for designing unimodular sequences with good correaltion properties," *IEEE Trans. Signal Process.*, vol. 57, no. 4, pp. 1415–1425, Apr. 2009.

[11] P. Stoica, H. He, and J. Li, "On designing sequences with impulse-like periodic correlation," *IEEE Signal Process. Lett.*, vol. 16, no. 8, pp. 703–706, Aug. 2009.

[12] J. Liang, L. Xu, J. Li, and P. Stoica, "On designing the transmission and reception of multistatic continuous active sonar systems," *IEEE Trans. Aerosp. Electron. Syst.*, vol. 50, no. 1, pp. 285–299, Jan. 2014.

[13] J. Song, P. Babu, and D. P. Palomar, "Optimization methods for designing sequences with low autocorrelation sidelobes," *IEEE Trans. Signal Process.*, vol. 63, no. 15, pp. 3998–4009, Aug. 2015.

[14] J. Liang, H. C. So, C. S. Leung, J. Li, and A. Farina, "Waveform design with unit modulus and spectral shape constraints via lagrange programming neural network," *IEEE J. Sel. Topics. Signal Process.*, vol. 9, no. 8, pp. 1377–1386, Dec. 2015.

[15] S. Zhang and A. G. Constantinides, "Lagrange programming neural networks," *IEEE Trans. Circuits. Syst. II, Analog Digit. Signal Process.*, vol. 39, no. 7, pp. 441–452, Jul. 1992.

[16] G. Cui, H. Li, and M. Rangaswamy, "MIMO radar waveform design with constant modulus and similarity constraints," *IEEE Trans. Signal Process.*, vol. 62, no. 2, pp. 343–353, Jan. 2014.

[17] O. Aldayel, V. Monga, and M. Rangaswamy, "SQR: Successive QCQP refinement for MIMO radar waveform design under practical constraints," in *Proc. Asilomar Conf. Signals, Syst. Comput.*, Pacific Grove, CA, USA, Nov. 2015, pp. 85–89.

[18] S. E. Kocabas and A. Atalar, "Binary sequences with low aperiodic autocorrelation for synchronization purposes," *IEEE Commun. Lett.*, vol. 7, no. 1, pp. 36–38, Jan. 2003.

[19] P. Borwein and R. Ferguson, "Polyphase sequences with low autocorrelation," *IEEE Trans. Inf. Theory*, vol. 51, no. 4, pp. 1564–1567, 2005.

[20] G. Wang and Y. Lu, "Sparse frequency transmit waveform design with soft power constraint by PSO algorithm," in *Proc. IEEE Radar Conf.*, Rome, Italy, May 2008, pp. 1–4.

[21] D. Gabay, "Applications of the method of multipliers to variational inequalities," *Augmented Lagrangina Methods: Applications to the Solution of Boundary-Value Problems.* Amsterdam, The Netherlands: North Holland, 1983.

[22] J. Eckstein and D. P. Bertsekas, "On the Douglas-Rachford splitting method and the proximal point algorithm algorithm for maximal monotone operators," *Math. Program.*, vol. 55, pp. 293–318, 1992.

[23] Y. Wang, J. Yang, W. Yin, and Y. Zhang, "A new alternating minimization algorithm for total variation image reconstruction," *SIAM J. Imag. Sci.*, vol. 1, pp. 248–272, 2008.

[24] S. Boyd, N. Parikh, E. Chu, B. Peleato, and J. Ecksein, "Distributed optimization and statistical learning via the alternating direction method of multipliers," *Found. Trends Mach. Learn.*, vol. 3, no. 1, pp. 1–122, 2011.

[25] T. Erseghe, "A distributed and maximum-likelihood sensor network localization algorithm based upon a nonconvex problem formulation," *IEEE Trans. Signal Inf. Process. Netw.*, vol. 1, no. 4, pp. 247–258, Dec. 2015.

[26] J. Liang, G. Yu, B. Chen, and M. Zhao, "Decentralized dimensionality reduction for distributed tensor data across sensor networks," *IEEE Trans. Neural Netw. Learn. Syst.*, vol. PP, no. 99, preprint, doi: 10.1109/TNNLS.2015.2469100.

[27] M. Hong, Z.-Q. Luo, and M. Razaviyayn, "Convergence analysis of alternating direction method of multipliers for a family of nonconvex problems," in *Proc. IEEE Int. Conf. Acoust., Speech, Signal Process.*, Brisbane, Australia, Apr. 2015, pp. 3836–3840.

[28] S. P. Boyd and L. Vandenberghe, *Convex Optimization*. Cambridge, U.K.: Cambridge Univ. Press, 2004.

[29] D. P. Bertsekas, *Constrained Optimization and Lagrange Multiplier Methods*. New York, NY, USA: Academic, 1982.

[30] H. Hotelling, "Some new methods in matrix calculation," *Ann. Math. Statist.*, vol. 14, pp. 1–34, 1943.

[31] H. Hotelling, "Further points on matrix calculation and simultaneous equations," *Ann. Math. Statist.*, vol. 14, pp. 440–441, 1943.

[32] J. W. Cooley and J. W. Tukey, "An algorithm for the machine calculation of complex Fourier series," *Math. Comput.*, vol. 19, pp. 297–301, 1965.

[33] S. Winograd, "On computing the discrete Fourier transform," *Math. Comput.*, vol. 32, no. 141, pp. 175–199, 1978.

[34] C. M. Rader, "Discrete Fourier transforms when the number of data samples is prime," *Proc. IEEE*, vol. 56, no. 6, pp. 1107–1108, Jun. 1968.

[35] H. Leong and B. Sawe, "Channel availability for east coast high frequency surface wave radar systems," Defence R D Canada, Ottawa, ON, Canada, Tech. Rep. DREO TR 2001–104, 2001.

Junli Liang (SM'16) was born in China. He received the Ph.D. degree in signal and information processing from the Institute of Acoustics, Chinese Academy of Sciences, Beijing, China. He is currently a Professor in the School of Electronics and Information, Northwestern Polytechnical University, China. His research interests include radar signal processing, image processing, and their applications.

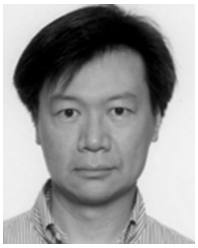

Hing Cheung So (S'90–M'95–SM'07–F'15) was born in Hong Kong. He received the B.Eng. degree from the City University of Hong Kong, Kowloon Tong, Hong Kong, and the Ph.D. degree from The Chinese University of Hong Kong, Hong Kong, both in electronic engineering, in 1990 and 1995, respectively. From 1990 to 1991, he was an Electronic Engineer in the Research and Development Division, Everex Systems Engineering Ltd., Hong Kong. During 1995–1996, he was a Postdoctoral Fellow at The Chinese University of Hong Kong. From 1996 to 1999, he was a Research Assistant Professor in the Department of Electronic Engineering, City University of Hong Kong, where he is currently a Professor. His research interests include detection and estimation, fast and adaptive algorithms, multidimensional harmonic retrieval, robust signal processing, source localization, and sparse approximation. He has been on the editorial boards of the *IEEE Signal Processing Magazine* (since 2014), the IEEE TRANSACTIONS ON SIGNAL PROCESSING (2010–2014), *Signal Processing* (since 2010), and *Digital Signal Processing* (since 2011). He is also a Lead Guest Editor of the IEEE JOURNAL OF SELECTED TOPICS IN SIGNAL PROCESSING MAGAZINE, special issue on "Advances in Time/Frequency Modulated Array Signal Processing." In addition, since 2011 he is an Elected Member in Signal Processing Theory and Methods Technical Committee of the IEEE Signal Processing Society, where since 2015 he has been the Chair in the awards subcommittee.

Jian Li (S'87–M'91–SM'97–F'05) received the M.Sc. and Ph.D. degrees in electrical engineering from The Ohio State University, Columbus, OH, USA, in 1987 and 1991, respectively. From April 1991 to June 1991, she was an Adjunct Assistant Professor in the Department of Electrical Engineering, The Ohio State University, Columbus. From July 1991 to June 1993, she was an Assistant Professor in the Department of Electrical Engineering, University of Kentucky, Lexington, KT, USA. Since August 1993, she has been in the Department of Electrical and Computer Engineering, University of Florida, Gainesville, FL, USA, where she is currently a Professor. In Fall 2007, she was on sabbatical leave at MIT, Cambridge, MA, USA. Her current research interests include spectral estimation, statistical and array signal processing, and their applications. She was an Associate Editor of the IEEE TRANSACTIONS ON SIGNAL PROCESSING from 1999 to 2005 and an Associate Editor of the IEEE SIGNAL PROCESSING MAGAZINE from 2003 to 2005. She is a Member of Sigma Xi and Phi Kappa Phi. She received the 1994 National Science Foundation Young Investigator Award and the 1996 Office of Naval Research Young Investigator Award. She was an Executive Committee Member of the 2002 International Conference on Acoustics, Speech, and Signal Processing, Orlando, Florida, May 2002. She was a Member of the Editorial Board of Signal Processing, a publication of the European Association for Signal Processing (EURASIP), from 2005 to 2007, a Member of the Editorial Board of the IEEE SIGNAL PROCESSING MAGAZINE from 2010 to 2012, and a Member of the Editorial Board of *Digital Signal Processing—A Review Journal*, a publication of Elsevier, from 2006 to 2012. She is currently a Member of the Sensor Array and Multichannel Technical Committee of the IEEE Signal Processing Society. She is a coauthor of the papers that have received the First and Second Place Best Student Paper Awards, respectively, at the 2005 and 2007 Annual Asilomar Conferences on Signals, Systems, and Computers in Pacific Grove, CA, USA. She is a Coauthor of the paper that has received the M. Barry Carlton Award for the best paper published in the IEEE TRANSACTIONS ON AEROSPACE AND ELECTRONIC SYSTEMS in 2005. She is a coauthor of the paper that has received the Lockheed-Martin Best Student Paper Award at the 2009 SPIE Defense, Security, and Sensing Conference in Orlando, FL, USA. She is also a coauthor of a paper published in the IEEE TRANSACTIONS ON SIGNAL PROCESSING that has received the Best Paper Award in 2013 from the IEEE Signal Processing Society. She is a Fellow of IET.

Alfonso Farina (LF'13) received the Laurea degree in EE from the University of Rome, Roma, Italy, in 1973. In 1974, he joined Selenia, now Selex ES, where he was the Director of the Analysis of Integrated Systems Unit and subsequently of the Engineering of Large Business Systems Division. In 2012, he was the Senior VP and Chief Technology Officer (CTO) of the company, reporting directly to the President. During 2013–2014, he was a Senior Advisor to CTO. He retired in October 2014. From 1979 to 1985, he was also a Professor of radar techniques at the University of Naples. He has provided innovative technical solutions to detection, signal-data-image processing, tracking, and fusion for the radar systems conceived, designed, and developed in the company. He has provided leadership in many projects, at the international level also, in surveillance for ground and naval applications, in airborne early warning, and in imaging radar. He is an author of more than 600 peer-reviewed technical publications and of books and monographs (published worldwide), some of them have also been translated in Russian and Chinese. He is currently consulting and teaching in radar, and is also a Distinguished Lecturer in the IEEE AESS, offering the following lecture: "Radar Adaptivity: Antenna Based Signal Processing Techniques." Currently, he is a Visiting Professor in the Department of Electronics, UCL, and also serves as an IEEE AESS BoG, a VP for Industry Relation, and as an Industry Advisory Chair CTIF (Center for TeleInFrastructures) (ctif-italy.uniroma2.it/). He received many awards, some of which are as follows: leader of the team that received the 2004 First Prize Award for Innovation Technology of Finmeccanica; International Fellow of the Royal Academy of Engineering, U.K. (2005): the Fellowship was presented to him by HRH Prince Philip, the Duke of Edinburgh; and IEEE Dennis J. Picard Medal for Radar Technologies and Applications (2010): ¡°for continuous, innovative, theoretical, and practical contributions to radar systems and adaptive signal processing techniques¡±. In 2014, he received a 2014 IET Achievement Medal ¡°for outstanding contributions to radar system design, signal, data and image processing, and data fusion¡±. He has been a Session Chairman at all the main international radar conferences held in the last 35 years. He is frequently invited to present papers at plenary sessions (more than 130 invited papers, presentations, plenary speeches) and tutorials (more than 16 in different countries) at international radar, signal processing, and fusion conferences. Main topics are adaptive radar SP, STAP, SAR, detection, tracking, and multisensor fusion. He is also an Invited Speaker at the NATO LS given in many countries (on SAR, STAP, KBS radar and WDD, etc.). He is one of the founders of the International Society for Information Fusion (ISIF); he has served on its BoD. He was an Executive General Chairman and a Plenary Speaker at International Fusion 2006 Conference in Florence. He was the organizer and the General Chairman of the 2008 IEEE-AESS Radar Conference in Rome, the first time that such conference was held outside U.S. More than 650 attendees from 40 countries registered at the conference: an all-time record for this premier conference series that has been organized annually since 1974. He is on the Editorial Board of a few international journals, including *IEE Proceedings—Radar, Sonar and Navigation* and Springer's *Signal, Image, and Video Processing*. He has established an effective, successful, and durable bridge between industry and academia, which provides both sides with advantages via the cross-fertilization of ideas and achievement of successful scientific and industrial results. He is a Fellow of REng, FIET, and EURASIP.